

Quantum Properties of Chaotic Systems

Submitted April 2025, in partial fulfillment of
the conditions for the award of the degree **MMath Mathematics**

Matthew Scargill

20331673

Supervisor: Dr Martin Richter

Assessment type: Investigation

Department of Mathematics

University of Nottingham

I have read and understood the School and University guidelines on plagiarism. I confirm that this work is my own, apart from the acknowledged references.

Abstract

This thesis explores the effect of classical chaos on the properties of quantum billiard systems. To address such systems, an understanding of boundary element methods (BEMs) is built up to implement a BEM in the Julia programming language. Boundary integral equations are constructed by deriving Green's representation theorem, and then evaluated for numerical robustness. The Nyström and Bubnov-Galerkin methods for approximating these equations are then detailed and compared. Our chosen implementation is used to produce the spectrum of resonant modes and create visualisations of bound states on the chosen billiard, used to analyse the role of symmetry. Concepts of classical chaos and the Weyl unfolding process required to compare the mode spectra of various billiards are discussed. Once done, the mode spacing density distributions of classically integrable and chaotic billiards are compared. Classically integrable billiards are shown to follow a Poisson distribution, while chaotic billiards are shown to tend towards a different distribution. This is determined to be the Gaussian Orthogonal Ensemble, a standard result from random matrix theory.

Acknowledgments

First and foremost, I would like to express my heartfelt thanks to my supervisor, Martin Richter, with whom it has been a pleasure to work. I am very thankful to my tutor Reuben O'Dea, whose dutiful quotations of Dumbledore have been an immeasurable help along the way. I'm also sincerely grateful to my friends and loved ones for their support and encouragement. Finally, I'd like to thank my Mum and Dad for more than I could ever count.

Contents

1	Introduction	3
2	Constructing Boundary Integral Equations	4
2.1	Representation as an integral	4
2.2	The problem along the boundary	6
3	Methods for Integral Equations	9
3.1	Comparative well-posedness of Fredholm equations	9
3.2	Numerical quadrature	12
3.2.1	The Nyström method	14
3.3	Finite Dimensional Compression	15
3.3.1	The Bubnov-Galerkin method	17
3.4	Practical considerations	18
4	Solving the Helmholtz eigenproblem	19
4.1	Resonant modes	19
4.2	Solutions to the Helmholtz equation	24
4.3	Symmetry and degenerate spectra	28
5	Spectral statistics	31
5.1	Liouville Integrability	31
5.2	Weyl's law and spectral unfolding	32
5.3	Integrable and chaotic systems	33
6	Random Matrix Theory	36
6.1	Constructing Wigner-Dyson distributions	36
6.2	Comparison to the spectra of chaotic systems	39
7	Conclusion and Outlook	40
A	Boundary Element Method code	42
B	Spectral Analysis code	47

1 Introduction

In a classical setting, billiard systems, where a particle propagates inside a bounded region, experiencing elastic collisions along the boundary, have long been a uniquely helpful class of systems when considering chaotic dynamics, as a careful choice of the boundary can produce regular, mixed, to strongly chaotic behaviour. The deep insights into chaos and Hamiltonian dynamics these systems provide have far-reaching applications, such as in transport theory [15], statistical mechanics [8], and weather forecasting [46, 18].

Billiard systems also present a fantastic opportunity to explore the concept of quantum chaos. Not only do they offer a clean and clear semi-classical limit, but they also allow for analogous microwave billiard experiments [60, 25]. Research into quantum chaos has already shown itself to be as dynamic as that of classical chaos, with notable applications in the fields of quantum computing [45, 50], optimisation of laser technology [67], and astrophysics [56]. In a quantum setting, the phase space trajectory definition of chaos loses meaning due to the Heisenberg uncertainty principle. The dynamics of quantum billiard systems are instead described by stationary wave functions ψ and associated resonant modes k , which combine to solve the Helmholtz equation [63]

$$(\Delta + k^2)\psi = 0. \tag{1}$$

In this thesis, we will investigate the classical limit of such systems, showing how classical chaos dictates quantum properties. The first half will be dedicated to outlining the theory of boundary element methods (BEMs) and implementing one in the Julia programming language [14]. We will consider aspects such as the well-posedness of the boundary integrals which arise and the computational efficiency of the quadrature methods used. Once we have completed our tool, we will use it to recover the spectrum of resonant modes and stationary solutions for generic billiards. We then discuss the notions of classical chaos to determine which billiards to compare, and the numerical conditioning required to make statistically relevant comparisons between them. With this, we compare the mode spacing density distributions of classically integrable and chaotic billiards, relating our findings to the field of random matrix theory.

2 Constructing Boundary Integral Equations

As outlined above, solutions and associated resonant modes for arbitrarily bounded billiard systems are given by the homogeneous Helmholtz equation (1). Since the boundaries of such systems are closed, the divergence theorem can be used to build a link between the bounded region Ω and its boundary $\partial\Omega$. That is the first task of this chapter: redefining our 2-dimensional partial differential on Ω as a 1-dimensional integral equation along the boundary $\partial\Omega$. By deriving Green's identities and considering the fundamental solutions of the Helmholtz equation, we find an expression which relates a function on a given region to an integral equation entirely defined along its boundary. This integral formulation is known as Green's representation theorem.

To completely prescribe our problem to the boundary, we describe the solution in terms of boundary data. This is done directly by taking the limit of the representation theorem approaching the boundary and applying known boundary conditions, leaving an equation in either the wave-function ψ or its normal derivative $\frac{\partial\psi}{\partial\mathbf{n}}$. The mathematically equivalent indirect method instead introduces an ansatz density function μ , used to define layer potentials along the boundary. These are heuristically selected to most easily conform to the boundary conditions and produce similar integral equations to the direct method. The results from both methods take the form of Fredholm equations of the first and second kind. These are known as Boundary Integral Equations (BIEs) as they produce boundary data which will be reintroduced into the representation theorem to determine solutions on Ω .

2.1 Representation as an integral

By requiring the boundaries of our billiard systems to be closed and piecewise continuous, they can be linked to their respective surfaces by the 2-dimensional divergence theorem (2). Let us consider a vector field of scalar functions on Ω of the form $F = \psi\nabla\phi$ for ψ, ϕ both twice continuously differentiable which transform as

$$\int_{\Omega} \nabla \cdot F \, dS = \int_{\Omega} \nabla \cdot [\psi \nabla \phi] \, dS = \int_{\partial\Omega} F \cdot d\mathbf{s}_y, \quad (2)$$

where $d\mathbf{s}_y = \mathbf{n} \cdot d\mathbf{s}_y$ is the line element and \mathbf{n} is the outward pointing unit normal. This expression is then simplified by the vector identity: $\nabla(\psi\alpha) = \nabla\psi\alpha + \psi\nabla\alpha$. By setting $\alpha = \nabla\phi$, we find Green's first identity

$$\int_{\Omega} \psi \Delta\phi + \nabla\psi \nabla\phi \, dS = \int_{\partial\Omega} \psi \nabla\phi \cdot d\mathbf{s}_y. \quad (3)$$

Here, and for the rest of the paper, we will write $\Delta = \nabla^2$. Since ψ and ϕ are both twice continuously differentiable, we can interchange them to form a new equation and subtract it from the original expression to eliminate the term in $\nabla\psi\nabla\phi$. Furthermore, the surface element can be decomposed and used to redefine

the derivatives in the RHS integral, as $\nabla\psi \cdot \mathbf{n}_y = \frac{\partial\psi}{\partial\mathbf{n}_y} = \nabla_{\mathbf{n}}$. These derivatives become outward-pointing directional derivatives of ψ , leading to Green's second identity

$$\int_{\Omega} \psi \Delta\phi - \phi \Delta\psi \, dS = \int_{\partial\Omega} \psi \nabla_n \phi - \phi \nabla_n \psi \, ds_y. \quad (4)$$

To rid ourselves of the integral over Ω , we must consider the fundamental solution of the Helmholtz equation. The fundamental solution of a linear differential operator L is a function F which satisfies

$$L F = \delta(x - x_0) \quad (5)$$

where $\delta(x - x_0)$ is the Dirac delta. These functions, in their many forms, are known as Green's functions [22, 19]. Since they are solutions to the boundary value problem (1), they normally depend on imposed boundary values. However, as shown in [64], we can use the Sommerfeld radiation condition

$$\lim_{r \rightarrow \infty} r^{1/2} \left(\frac{\partial\psi}{\partial r} - ik\psi \right) = 0, \quad (6)$$

where r is the radial coordinate from a scattering source, to define unique solutions to (5). This condition implies that solutions should behave like outgoing plane waves at infinity, which is the physically meaningful choice in the case of scattering. In the case where $L = \Delta + k^2$ in 2 dimensions, this leads us to the 2-dimensional "free-space" Green's function

$$G_k(\mathbf{r}, \mathbf{r}') = \frac{i}{4} H_0^{(1)}(k|\mathbf{r} - \mathbf{r}'|), \quad (7)$$

where $H_0^{(1)}$ is the Hankel function of the first kind and order 0. As a fundamental solution, G (we drop the subscript for clarity) is defined such that

$$(\Delta + k^2)G = \delta(x - x_0).$$

Expanding the Helmholtz equation into $\Delta\psi = -k^2\psi$, we're now equipped to derive Green's third identity. By applying Green's second identity (4) with $\psi(x)$ a solution of $Lu = 0$ on Ω and $\phi = G(x, r_y)$, and substituting our expression for $\Delta\psi$ into the LHS, we derive Green's third identity, more commonly known as Green's representation theorem [20]:

$$\psi(x) = \int_{\partial\Omega} G(x, r_y) \nabla_n \psi(r_y) - \psi(r_y) \nabla_n G(x, r_y) \, ds_y \quad (8)$$

Note the key feature of this expression: the only remaining integral is entirely defined along the boundary, as required. Furthermore, both terms on the right-hand side contain only one of either ψ or $\nabla_n \psi$ defined along the boundary.

2.2 The problem along the boundary

For our problem to be completely prescribed to the boundary, it must be expressed in terms of boundary data. This is done either by taking the limit of the representation theorem as $x \in \Omega$ tends to a point r_x on the boundary $\partial\Omega$

$$\lim_{x \rightarrow r_x} \psi(x) = \lim_{x \rightarrow r_x} \int_{\partial\Omega} G(x, r_y) \frac{\partial \psi}{\partial \mathbf{n}}(r_y) - \psi(r_y) \frac{\partial G(x, r_y)}{\partial \mathbf{n}_y} ds_y \quad r_x \in \partial\Omega, \quad (9)$$

or by first taking the normal derivative with respect to x and then taking the same limit as above

$$\lim_{x \rightarrow r_x} \frac{\partial \psi}{\partial \mathbf{n}}(x) = \lim_{x \rightarrow r_x} \int_{\partial\Omega} \frac{\partial G(x, r_y)}{\partial \mathbf{n}_x} \frac{\partial \psi}{\partial \mathbf{n}}(r_y) - \psi(r_y) \frac{\partial^2 G(x, r_y)}{\partial \mathbf{n}_x \partial \mathbf{n}_y} ds_y \quad r_x \in \partial\Omega, \quad (10)$$

where we have expanded ∇_n to distinguish the effect of different partial derivatives on G . This distinction is not required in the case of ψ as it is not multivariate. In both cases, which we shall address separately, we will redefine each of the integral terms as boundary integral operators.

In (9), the term in ψ is known as the double layer potential, representing the "sound-soft" properties of the boundary. To circumvent discontinuity as we cross $\partial\Omega$, we introduce a well-known jump term [42, 1]. Since we require $\partial\Omega$ to be piecewise continuous, we simply set this term to $\frac{1}{2}$, the sign of which depends on whether x approaches the boundary externally or from within. In our internal case, we take

$$[\frac{1}{2}\psi - D\psi](r_x) = - \lim_{x \rightarrow r_x} \int_{\partial\Omega} \psi(r_y) \frac{\partial G(x, r_y)}{\partial \mathbf{n}_y} ds_y$$

where

$$[D\psi](r_x) = \int_{\partial\Omega} \psi(r_y) \frac{\partial G(r_x, r_y)}{\partial \mathbf{n}_y} ds_y$$

is known as the double layer potential operator. Physically, this represents boundary data as the effect of dipole-like sources along $\partial\Omega$. The term in $\frac{\partial \psi}{\partial \mathbf{n}}$ is the single layer potential, which accounts for the "sound-hard" properties of the boundary and can be interpreted as having charge-like point sources along it. Since it is continuous when passing across the boundary, the single-layer potential is expressed by the boundary

operator

$$[S \frac{\partial \psi}{\partial \mathbf{n}}](r_x) = \lim_{x \rightarrow r_x} \int_{\partial \Omega} G(x, r_y) \frac{\partial \psi}{\partial \mathbf{n}}(r_y) \, ds_y = \int_{\partial \Omega} G(r_x, r_y) \frac{\partial \psi}{\partial \mathbf{n}}(r_y) \, ds_y.$$

Expressed entirely in terms of boundary operators, our representation theorem takes the form

$$\psi(r_x) = [S \frac{\partial \psi}{\partial \mathbf{n}}](r_x) + [\frac{1}{2} \psi - D\psi](r_x). \quad (11)$$

For (10), analogous operators arise from the normal derivatives of the single and double layer potential operators. While they can retain their physical interpretations as point sources and dipoles respectively, their continuity when crossing $\partial \Omega$ and thus jump formulas are reversed. From the double layer potential, we derive the hypersingular boundary operator

$$[H\psi](r_x) = \lim_{x \rightarrow r_x} \int_{\partial \Omega} \psi(r_y) \frac{\partial^2 G(x, r_y)}{\partial \mathbf{n}_x \partial \mathbf{n}_y} \, ds_y.$$

which is continuous when passing across $\partial \Omega$, not requiring a jump term. Conversely, the single layer potential defines the adjoint double layer potential and its boundary operator W as

$$\left[\frac{1}{2} \frac{\partial \psi}{\partial \mathbf{n}} + W \frac{\partial \psi}{\partial \mathbf{n}} \right] (r_x) = \lim_{x \rightarrow r_x} \int_{\partial \Omega} \frac{\partial G(x, r_y)}{\partial \mathbf{n}_x} \frac{\partial \psi}{\partial \mathbf{n}}(r_y) \, ds_y$$

and

$$[W \frac{\partial \psi}{\partial \mathbf{n}}](r_x) = \int_{\partial \Omega} \frac{\partial G(r_x, r_y)}{\partial \mathbf{n}_x} \frac{\partial \psi}{\partial \mathbf{n}}(r_y) \, ds_y.$$

These new operators allow us to write our representation theorem as

$$\frac{\partial \psi}{\partial \mathbf{n}_x}(r_x) = [\frac{1}{2} \frac{\partial \psi}{\partial \mathbf{n}} + W \frac{\partial \psi}{\partial \mathbf{n}}](r_x) - [H\psi](r_x). \quad (12)$$

To provide solutions to these equations, we must impose boundary values. Dirichlet conditions, where $\psi = 0$ along $\partial \Omega$, are most commonly considered when working with billiard systems, but the above formulation also allows for easy application of Neumann boundary conditions where $\frac{\partial \psi}{\partial \mathbf{n}} = 0$. These are especially advantageous as resulting operators are self-adjoint and thus produce a real and positive spectrum of k [33]. In either case, it is clear that one of the boundary operators in each of (9) and (10) vanishes. Imposing Dirichlet conditions eliminates both the double layer potential and the LHS of (9) and the hypersingular layer potential in (10), leaving

$$\int_{\partial \Omega} G(r_x, r_y) \frac{\partial \psi}{\partial \mathbf{n}}(r_y) \, ds_y = 0 \quad (13)$$

and

$$\frac{1}{2} \frac{\partial \psi}{\partial \mathbf{n}}(r_x) = \int_{\partial \Omega} \frac{\partial G(r_x, r_y)}{\partial \mathbf{n}_x} \frac{\partial \psi}{\partial \mathbf{n}}(r_y) \, ds_y. \quad (14)$$

Similarly, Neumann conditions eliminate the single layer potential in (9), and the adjoint double layer potential and LHS of (10). This leaves

$$\frac{1}{2} \psi(r_x) = - \int_{\partial \Omega} \psi(r_y) \frac{\partial G(r_x, r_y)}{\partial \mathbf{n}_y} \, ds_y \quad (15)$$

and

$$\int_{\partial \Omega} \psi(r_y) \frac{\partial^2 G(r_x, r_y)}{\partial \mathbf{n}_x \partial \mathbf{n}_y} \, ds_y = 0. \quad (16)$$

Both the above formulations form the "direct" method, as they produce formulations of the Dirichlet and Neumann eigenproblems in terms of the unknown physical quantities ψ and $\frac{\partial \psi}{\partial \mathbf{n}}$. In contrast, the "indirect" method involves the a priori assumption that the solution to the Helmholtz equation will take on the shape of a known potential layer. In practice, this involves introducing an ansatz auxiliary density function μ which is solved for and used in the same way as above. We first make the heuristic choice of

$$\begin{aligned} \mu(x) &= \int_{\partial \Omega} G(x, r_y) \mu(r_y) \, ds_y \\ \mu(x) &= \int_{\partial \Omega} \frac{\partial G(x, r_y)}{\partial \mathbf{n}_y} \mu(r_y) \, ds_y \\ \mu(x) &= \int_{\partial \Omega} \frac{\partial G(x, r_y)}{\partial \mathbf{n}_x} \mu(r_y) \, ds_y \\ \mu(x) &= \int_{\partial \Omega} \frac{\partial^2 G(x, r_y)}{\partial \mathbf{n}_x \partial \mathbf{n}_y} \mu(r_y) \, ds_y \end{aligned}$$

then take the limit as $x \rightarrow r_x \in \partial \Omega$ and apply appropriate jump conditions as above. This leads to equivalent equations in μ [40].

Both methods result in Boundary Integral Equations (BIEs), solvable equations which produce the boundary data of either ψ or $\frac{\partial \psi}{\partial \mathbf{n}}$ [35] which can be reinserted into (8). With this new, more computationally viable formulation of the Helmholtz eigenproblem, the first step of the BEM is complete. Depending on the choice of formulation and boundary conditions, BIEs take the form of homogeneous Fredholm equations of the first or second kind [70]. From here we will only consider the case of Dirichlet boundary conditions, working with equations (13) and (14). Assessing and comparing the numerical stability of these equations will be the first concern of Chapter 3.

3 Methods for Integral Equations

So far, without loss of generality of the billiard boundary $\partial\Omega$, we have converted the Helmholtz eigenvalue problem into a choice of homogeneous Fredholm equation

$$\int_{\partial\Omega} G(r_x, r_y) \frac{\partial\psi}{\partial\mathbf{n}}(r_y) \, ds_y = 0 \qquad \frac{1}{2} \frac{\partial\psi}{\partial\mathbf{n}}(r_x) = \int_{\partial\Omega} \frac{\partial G(r_x, r_y)}{\partial\mathbf{n}_x} \frac{\partial\psi}{\partial\mathbf{n}}(r_y) \, ds_y.$$

of the first or second kind in $\frac{\partial\psi}{\partial\mathbf{n}}$ respectively. As such, our first duty in this chapter is to investigate the well-posedness of both. They display similarities in terms of existence and uniqueness, but differ enormously in terms of stability. Fredholm equations of the second kind are shown to be better numerically conditioned, and so we will turn our attention to solving these problems primarily.

For our purposes, we require 2 things from our approximation methods. The first is that the BIE be converted into a matrix equation of the form $B\phi = 0$. This allows for easier computational evaluation of resonant frequencies, as for such frequencies B is not invertible [71] and displays properties such as $\det(B) = 0$ and thus lowest singular values equal to 0. The second is that we require methods which can be efficiently and accurately scaled to access the eigenmode statistics of high energy levels. To these ends, we shall explore quadrature methods wherein the boundary $\partial\Omega$ is discretised and evaluated along this discretisation. The simplest choice is numerical integration using the Nyström method. Here, the solution is approximated by a weighted sum of functions evaluated at discretisation nodes; this method interacts with the equation in a point-wise sense. The weights and distribution of these nodes are determined by the choice of quadrature [69]. After this, we explore the Bubnov-Galerkin method of projecting the problem onto a finite-dimensional subspace of piecewise-constant functions, which discretise the boundary. This "weak" formulation is done by defining a bivariate form which contrasts the equation with this basis, producing an equivalent linear system which is used to reconstruct an approximation of the solution. Examples of both of these discretisation schemes are illustrated in Fig. 1. Here, we can imagine the Bubnov-Galerkin method concerning itself with integrals along the line segments between nodes, and the Nyström method concerning itself with the nodes themselves [28]. These methods are contrasted and compared in the contexts of numerical accuracy and computational efficiency.

3.1 Comparative well-posedness of Fredholm equations

Existence and Uniqueness The homogeneous nature of these equations introduces trivial solutions $g(x) = 0$ to both kinds of equations. More importantly, they also allow for nontrivial solutions at certain specific frequencies. In our case, these frequencies are the physically viable values of k and represent the

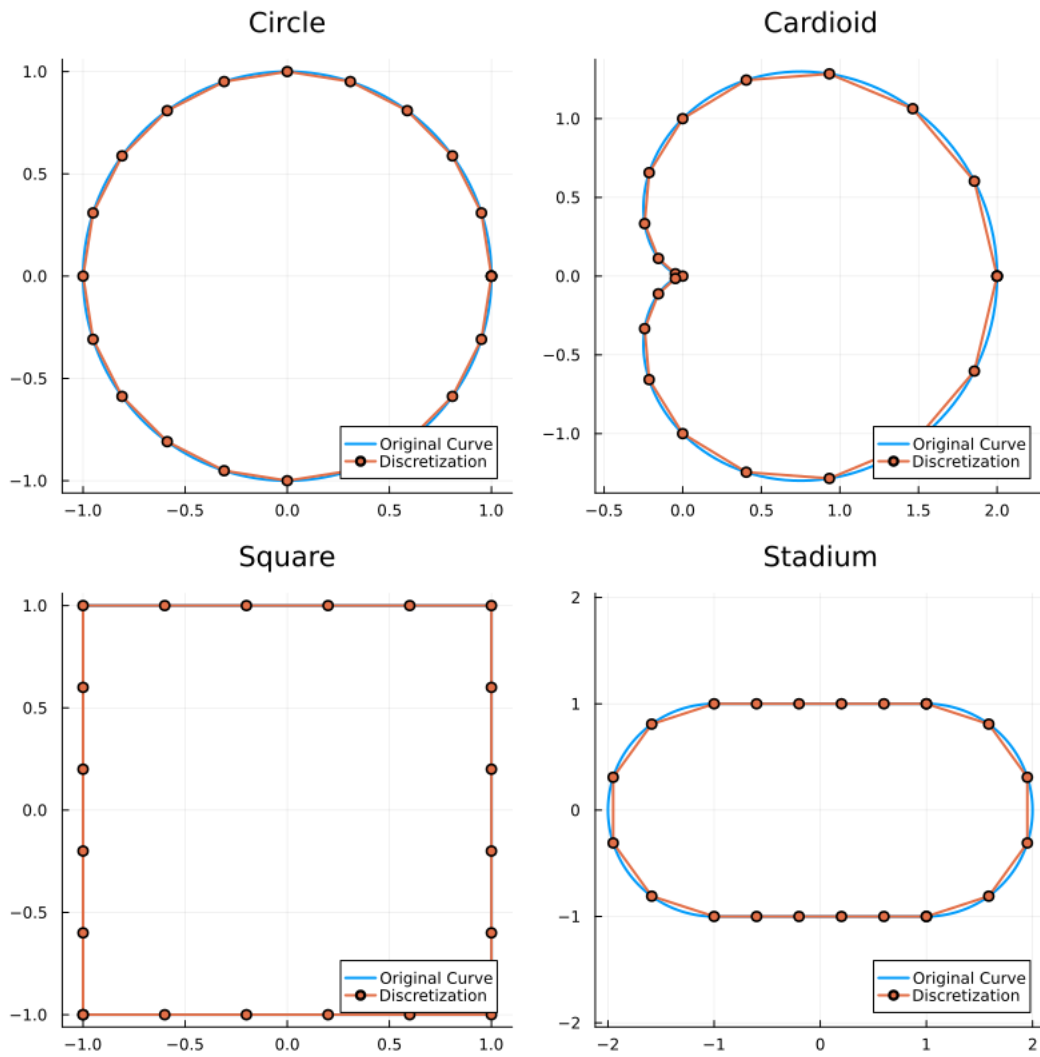


Figure 1: Visualisation of both point and segment discretisation schemes with $N = 20$

eigenmodes of our system. In the context of our eigenproblems

$$\mathcal{K}g = 0 \qquad (I - \mathcal{K})g = 0$$

where

$$[\mathcal{K}g](x) = \int K(x, y)g(y)dy,$$

these frequencies are those at which \mathcal{K} and $(I - \mathcal{K})$ become non-invertible. In other words, when 0 is an eigenvalue of these operators. In the case of equations of the second kind, this is equivalent to \mathcal{K} having eigenvalue 1. This is advantageous as it can be hard to distinguish eigenvalues as they often cluster around 0. This is our first indication of numerical instability in equations of the first kind.

Numerical stability The standard measure of stability is known as conditioning, which represents sensitivity to small errors and changes in input. Good conditioning as we increase the frequency k and the number of function space elements N is crucial. Here, we will apply a uniform quadrature scheme to a circular billiard to discretise both \mathcal{K} and $(I - \mathcal{K})$ into $N \times N$ matrix operators, allowing us to evaluate their well-posedness as linear operators. The kernel $K(x, y)$ of both is taken to be the 2-dimensional "free-space" Green's function for insight into our specific problem. The simplest indicator of stability is the condition number κ , which measures the inaccuracy of a solution x of a linear equation $Ax = b$ after approximation. This is defined as

$$\kappa(A) = \frac{\sigma_{\max}(A)}{\sigma_{\min}(A)} \tag{17}$$

where $\sigma_{\max}(A)$ and $\sigma_{\min}(A)$ are the largest and smallest singular values of A respectively. Condition numbers which stay small, ie. $\kappa \approx 1$ as k and N increase, are favourable as they indicate that the small errors introduced by quadrature are not detracting from the accuracy of the solution. Another method to consider is that of singular value decay. Singular values are a measure of how close a matrix is to being singular; if they are close to 0, then the matrix is close to being singular and thus very prone to numerical inaccuracies. In figure 2, we evaluate the condition number for N up to 200. We also compute the decay of singular values for $N = 200$. Both of these are done for frequencies 1, 80, and 150. For clarity, only every tenth singular value is plotted.

Fredholm equations of the second kind preserve a low conditioning number as both k and N rise. In contrast, equations of the first kind behave erratically when k happens to be too close to N . This is due to the oscillatory nature of the Green's function, a property carried by its normal derivative. With the wavelength being defined as $\lambda = \frac{2\pi}{k}$, it's clear that wild oscillations appear in conjunction with an increase in k . This

behaviour is mitigated by increasing N as shown in the second condition graph. However, the condition number still rises steadily. As we noted in the previous section, Fredholm equations of the first kind have their eigenvalues clustered around 0. Across the singular value decay graphs, we see that this collapse towards 0 is exacerbated at higher and higher frequencies. The stabilising influence of the identity operator mitigates both of these effects. In conclusion, homogeneous Fredholm equations of the second kind have shown themselves to be better posed problems and more computationally viable than those of the first kind. As such, we turn our attention exclusively to this formulation of the BIE.

3.2 Numerical quadrature

The simplest form of numerical integration, quadrature methods estimate definite integrals using a finite set of evaluation points. Here, we discretise the contour of the boundary $\partial\Omega$ into nodes with associated weights given by our choice of quadrature. This allows us to write the integral of a function as

$$\int_{\partial\Omega} g(y) dy \approx \sum_{i=1}^N w_i g(y_i) = w_1 g(y_1) + w_2 g(y_2) + \dots$$

with weights w_i associated to nodes y_i [51].

Example of weighted quadrature method An easy 1-dimensional example to consider is that the trapezoidal quadrature rule applied to the integral equation

$$\int_0^2 (x^2 + 1) dx \quad x \in [0, 2].$$

For this method, we must first generate equally distributed nodes along $[0, 2]$ with a specified step length h . Taking h to be 0.5, we generate the nodes

$$x_0 = 0, \quad x_1 = 0.5, \quad x_2 = 1.0, \quad x_3 = 1.5, \quad x_4 = 2.0.$$

Next, we insert these nodes into the 5-point trapezoidal rule formula

$$\int_a^b f(x) dx \approx \frac{h}{2} [f(x_0) + 2f(x_1) + 2f(x_2) + 2f(x_3) + f(x_4)].$$

In our case, where $f(x) = x^2 + 1$, we find

$$\int_a^b f(x) dx \approx \frac{1}{4} [f(0) + 2f(0.5) + 2f(1.0) + 2f(1.5) + f(2.0)] = \frac{1}{4} (1 + 2.5 + 4 + 6.5 + 5) = 4.75.$$

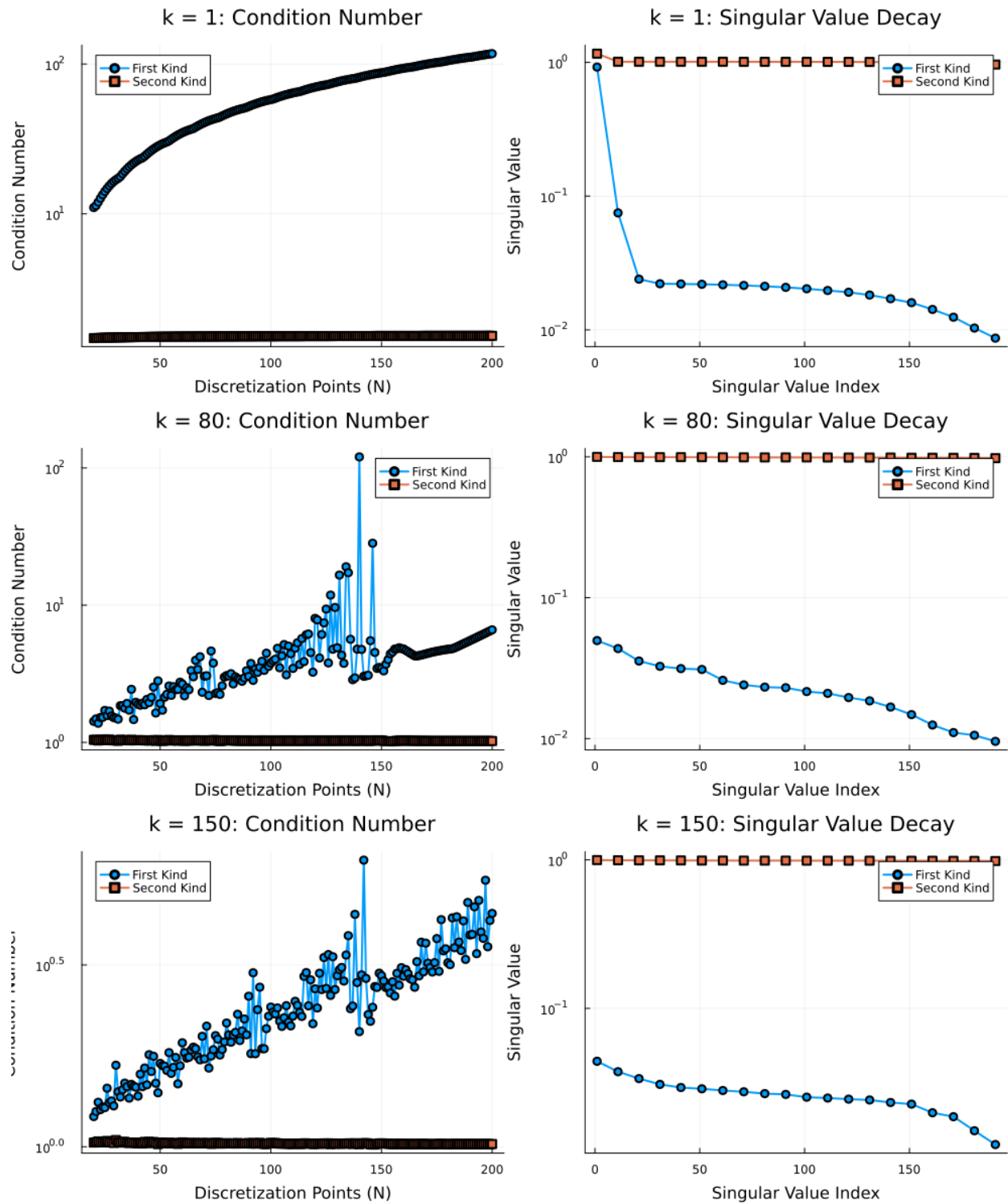


Figure 2: Evolution of condition number and singular value decay for discretization up to, and at, 200 nodes at $k = 1, 80, 150$.

Comparing this to the exact solution of 4.6667, we find an error of 0.0833, which tends to 0 as the number of evaluation nodes increases [57].

3.2.1 The Nyström method

This sum expansion of integrals allows us to express homogeneous Fredholm equations of the second kind as

$$g(x_j) - \sum_{i=1}^N K(x_j, y_i) w_i g(y_i) = 0$$

with x also discretised along the boundary to allow for a matrix formulation. However, this cannot be converted to a properly posed eigenproblem of the form $(I - \mathcal{K})g = 0$ unless $g(x_j) = g(x_i)$ for $i = j$. In other words, we must use the same set of boundary nodes to discretise both x and y . Accepting this stipulation, the BIE can be expressed as an eigenproblem with I the $N \times N$ identity matrix and \mathcal{K} a matrix of the same size with entries

$$\mathcal{K}_{ij} = w_i K(x_j, y_i).$$

Constructing this linear system from weighted quadrature approximations is known as the Nyström method [24]. Unfortunately, applying this method to our BIE is not as simple, as complications arise from reusing quadrature nodes. In our case, the kernel is the normal derivative of the 2-dimensional free-space Green's function

$$\frac{\partial G(k|\mathbf{x} - \mathbf{y}|)}{\partial \mathbf{n}_x} = \frac{\partial}{\partial \mathbf{n}_x} \left(\frac{i}{4} H_0^{(1)}(k|\mathbf{x} - \mathbf{y}|) \right) = -\frac{ik}{4} H_1^{(1)}(k|\mathbf{x} - \mathbf{y}|) \frac{\mathbf{x} - \mathbf{y}}{|\mathbf{x} - \mathbf{y}|} \cdot \mathbf{n}_x \quad (18)$$

where $H_1^{(1)}(k|\mathbf{x} - \mathbf{y}|)$ is the Hankel function of the first kind and order 1. Using the asymptotic approximation for $H_1^{(1)}(k|\mathbf{x} - \mathbf{y}|)$ where $|\mathbf{x} - \mathbf{y}| \rightarrow 0$, we see

$$H_1^{(1)}(k|\mathbf{x} - \mathbf{y}|) \approx -\frac{2i}{\pi k|\mathbf{x} - \mathbf{y}|} + \mathcal{O}(k|\mathbf{x} - \mathbf{y}| \ln k|\mathbf{x} - \mathbf{y}|). \quad (19)$$

To a leading order, this causes a $\frac{1}{|x|}$ -type singularity, leading to difficulty in taking this method further. Although specialised quadrature schemes do exist which can analytically extend this method to singular integrals [52, 17, 53], we can make the crude but sufficient [6] approximation of evaluating the kernel at the midpoints of our discretisation. In this case, we take the diagonal terms as the $\frac{1}{2}$ jump term described in Chapter 1 [6]. As a matrix equation $B\phi = 0$ where ϕ is the normal derivative of the wave function along the

boundary, this method defines the entries of B as

$$B_{ij} = \begin{cases} -w_i \frac{ik}{4} H_1^{(1)}(k|\mathbf{x}_i - \mathbf{y}_j|) \frac{\mathbf{x}_i - \mathbf{y}_j}{|\mathbf{x}_i - \mathbf{y}_j|} \cdot \mathbf{n}_x & i \neq j \\ \frac{1}{2} & i = j \end{cases} \quad (20)$$

where \mathbf{x}, \mathbf{y} are now defined as the midpoints between the nodes of our original quadrature.

3.3 Finite Dimensional Compression

The second option we consider is Rayleigh-Ritz methods, which originated in the context of boundary value problems like ours. These methods aim to approximate infinite-dimensional linear operators by finite-dimensional compressions. In practice, we seek to approximate a linear operator T on a Hilbert space \mathcal{H} as an equivalent solvable linear system of equations. This is done by projecting T onto the space spanned by a finite set of functions $V = \{\varphi_1, \dots, \varphi_n\}$ using the inner product (\cdot, \cdot) on \mathcal{H} . The resulting approximation T_V is the matrix

$$(T_V)_{ij} = (T\varphi_i, \varphi_j)$$

known as the *compression* of T to V [28]. In the context of Fredholm equations of the second kind, our eigenvalue problem can be written symbolically as

$$(I - \mathcal{K})g = 0,$$

having defined I as the identity and \mathcal{K} as a general integral operator. Let $V = \{\varphi_1, \dots, \varphi_n\}$ and assume

$$g(x) = \sum_{n=0}^N \alpha_n \varphi_n(x), \quad x \in \partial\Omega. \quad (21)$$

By projecting (equation $(I - \mathcal{K})g$) onto V , it is then equivalent to solving for α_i in the linear system

$$\sum_{n=0}^N \alpha_n \{(\varphi_i \varphi_n) - (\varphi_i \mathcal{K}(x, y), \varphi_n)\} = 0.$$

Expressed as the matrix equation $B_{ij}\alpha_i = 0$, the entries of B_{ij} take the form

$$B_{ij} = ((I - \mathcal{K})_V)_{ij} = (\varphi_i, \varphi_j) - (\mathcal{K}\varphi_i, \varphi_j) = \int \bar{\varphi}_i(x) \varphi_j(x) \, dx - \int \int K(x, y) \bar{\varphi}_i(y) \varphi_j(x) \, dy dx. \quad (22)$$

Example of projection-based method Let's consider the following Fredholm equation in the unknown function $g(x)$ on the interval $[0, 1]$:

$$g(x) - \lambda \int_0^1 (xy)g(y) \, dy = 0 \quad x \in [0, 1].$$

Here, λ is the eigenvalue of the integral operator defined by our kernel xy . We aim to approximate $g(x)$ as a finite linear combination of known basis functions. For simplicity, we will pick an orthonormal basis produced by the Gram-Schmidt process applied to $\{1, x\}$

$$\varphi_1(x) = 1 \quad \varphi_2(x) = \sqrt{12}\left(x - \frac{1}{2}\right)$$

with the aim to write the unknown function as

$$g(x) = \alpha_1 \varphi_1(x) + \alpha_2 \varphi_2(x) = \alpha_1 + \alpha_2 \sqrt{12}\left(x - \frac{1}{2}\right).$$

We can now express this as a linear system of the form $A\alpha = \lambda B\alpha$ with λ as an eigenvalue. The components of A and B can be written as

$$A_{ij} = \int_0^1 \psi_i(x) \psi_j(x) \, dx \quad B_{ij} = \int_0^1 \psi_i(x) \left(\int_0^1 x y \psi_j(y) \, dy \right) \, dx.$$

However, since we're working in an orthonormal basis, A is simply equivalent to the identity matrix. B is computed as

$$B = \begin{bmatrix} \int_0^1 \int_0^1 xy \, dx dy & \int_0^1 \int_0^1 xy \sqrt{12}(y - \frac{1}{2}) \, dx dy \\ \int_0^1 \sqrt{12}(x - \frac{1}{2}) \int_0^1 xy \, dx dy & \int_0^1 \sqrt{12}(x - \frac{1}{2}) x dx \int_0^1 \sqrt{12}(y - \frac{1}{2}) y dy \end{bmatrix} = \begin{bmatrix} 1/4 & \sqrt{3}/12 \\ \sqrt{3}/12 & 1/12 \end{bmatrix}.$$

From here, solving this system is an exercise in matrix manipulation, which leaves $\alpha = [\sqrt{3}, 1]^T$ with eigenvalue $\lambda = 3$, approximating our unknown function as

$$g(x) = \sqrt{3} + \sqrt{12}\left(x - \frac{1}{2}\right) = \sqrt{12}x.$$

Substituting this back into our expression, we find

$$\sqrt{12}x - 3 \int_0^1 xy(\sqrt{12}y) \, dy = \sqrt{12} - 3\sqrt{12}x \int_0^1 y^2 \, dy = \sqrt{12}x - \sqrt{12}x = 0$$

as required.

3.3.1 The Bubnov-Galerkin method

The choice of function space is paramount. Common choices are the orthonormal basis of T itself or functions which approximate the eigenfunctions of the spectrum. We will seek to discretise our boundary using a finite set of piecewise constant functions. This orthonormality-based formulation is known as Galerkin's method [24, 37, 3]. Primarily, this method comes in 2 flavours. The first is called the Petrov-Galerkin method, where new trial functions are introduced to approximate the unknown function. The second, which we will focus on, is called the Bubnov-Galerkin method, where basis functions of V are reused to this end (as in the above example).

Similarly to the Nyström method, the matrix elements produced by the Bubnov-Galerkin method (22) display singularities along the diagonal B_{ii} . However, unlike the Nyström method, these singularities are integrated over and not inherent. In some formulations of the BIE, they are weak singularities such as $\ln(x)$ [23, 65], which can be regularised and integrated over using methods such as Duffy integration [58]. These methods are unfortunately inaccessible since our chosen BIE presents a strong $\frac{1}{|x|}$ -type singularity. We can, however, still assign a Cauchy principal value to the inner integrals of these diagonal terms

$$\int_c^d \frac{\partial H_0^{(1)}}{\partial \mathbf{n}_x}(k|\mathbf{x} - \mathbf{y}|)d\mathbf{y}. \quad (23)$$

Here, we are integrating over the interval which contains a singularity at $\mathbf{y} = \mathbf{x}$. Let's focus on that singularity directly by introducing a parametrised expansion

$$\mathbf{y}(s) = \mathbf{x} + \mathbf{t}s + \frac{\kappa}{2}\mathbf{n}s^2 + O(s^3), \quad (24)$$

of \mathbf{y} around \mathbf{x} in local coordinates s , where $\mathbf{y}(0) = \mathbf{x}$ [26, 48]. In this expression, \mathbf{t} is the tangent vector, \mathbf{n} is the normal, and κ is the curvature of the boundary, all evaluated at \mathbf{x} . However, since we have discretised the boundary in terms of straight line segments, we note that $\mathbf{n} \cdot \mathbf{t} = 0$ and $\mathbf{y}(s) = -s\mathbf{t}$ since $\kappa = 0$. This, along with the fact that $\frac{\partial}{\partial \mathbf{n}_x} = \mathbf{n} \cdot \frac{d}{dx}$, allows us write (18) as

$$\frac{\partial H_0^{(1)}(k|-s\mathbf{t}|)}{\partial \mathbf{n}_x} = (-k)H_1^{(1)}(k|-s\mathbf{t}|)\frac{-s}{|-s\mathbf{t}|}\mathbf{t} \cdot \mathbf{n} = 0 \quad (25)$$

Since this result holds identically for all s , we say that the principal value of (23) is 0. As such, we take the entries along the diagonal of our Bubnov-Galerkin matrix as simply the $\frac{1}{2}$ contributions from the jump term.

Finally, we can describe our matrix operator B as

$$B_{ij} = \begin{cases} -\frac{i}{4} \int \int \frac{\partial H_0^{(1)}}{\partial \mathbf{n}_x}(k|\mathbf{x} - \mathbf{y}|) \, d\mathbf{y} d\mathbf{x} & \text{for } i \neq j \\ \frac{1}{2} & \text{for } i = j \end{cases} \quad (26)$$

3.4 Practical considerations

The Bubnov-Galerkin method imposes a weak form of the integral, which tends to lead to improved accuracy and robustness. It is also more broadly applicable when considering complex boundaries [4]. As such, convergence theory for Galerkin methods in general is better developed [44]. However, this is in exchange for comparatively very high computational cost to collocation methods such as Nyström. Early attempts to use the QuadGK [38] package for Julia lead to compute times which were unacceptable considering the brute force nature of searching for resonances detailed in Chapter 4. In contrast, the midpoint approximation of the Nyström method allows for fast matrix construction and high accuracy with relatively little computational effort. Unfortunately, this accuracy is more susceptible to degradation than that of Bubnov-Galerkin due to the oscillatory nature of BIE kernels. However, as we shall see, this approximation is sufficiently accurate for the objectives of this thesis.

4 Solving the Helmholtz eigenproblem

Expressed as the matrix equation $B\phi = 0$, the Helmholtz equation is not only more computationally viable, but solutions have clear conditions for both existence and uniqueness. As discussed above and in Chapter 3, the matrix operator B displays the equivalent properties

$$\det(B) = 0 \qquad \qquad \qquad \sigma_n(B) = 0 \qquad \qquad \qquad (27)$$

for physical solutions. As such, the first aim of this chapter is to leverage these properties to approximate the resonant modes of the system. To judge the accuracy of our method, we compare our approximations for the square and circle billiards to their analytically determined modes. Our second aim is to recover boundary data $\frac{\partial\psi}{\partial\mathbf{n}}$ from each of these eigenmodes using the matrix equation. This data is then introduced into the representation function (8) to reconstruct solutions of the Helmholtz equation on Ω . We attempt to replicate the results of Kaufman et al. [39] to gauge the fidelity of our approximated solutions. Finally, we explore the effect of symmetry on billiard diagrams and eigenmode spectra. The main functions of our implementation and a given example can be found in Appendix A.

4.1 Resonant modes

As mentioned above and in Chapter 3, resonant modes are defined by (27), where the determinant and lowest singular value of the matrix operator B are equal to 0. These conditions ensure the existence and uniqueness of solutions away from $\phi = 0$. To approximate these frequencies computationally, we consider a range of k spanned by n evaluation points. An evaluated frequency k_n is taken to be resonant if $\det(B(k_n))$ and $\sigma_n(B(k_n))$ are close to 0. To aid in the estimation of these eigenmodes and stave off high-frequency decay, we introduce the additional requirement that k_n be a local minimum to be considered resonant. This can be done as both the determinant and minimum singular value can be shown to be continuous functions of k [55]. This method has been implemented to graph the evolution of the minimum singular values of the circle and square billiards in Fig. 3 and 4, respectively. The approximated resonant frequencies have been marked on these figures by red dots, and the numerical values of the first 10 are recorded in Table 1.

To see how well our approximation fares, we derive and compare the analytic solutions for the circle and square billiards below. These systems are known as "integrable" as they possess strong symmetries which allow them to be solved via separation of variables. We will properly define and explore the notion of integrability in Chapter 5.

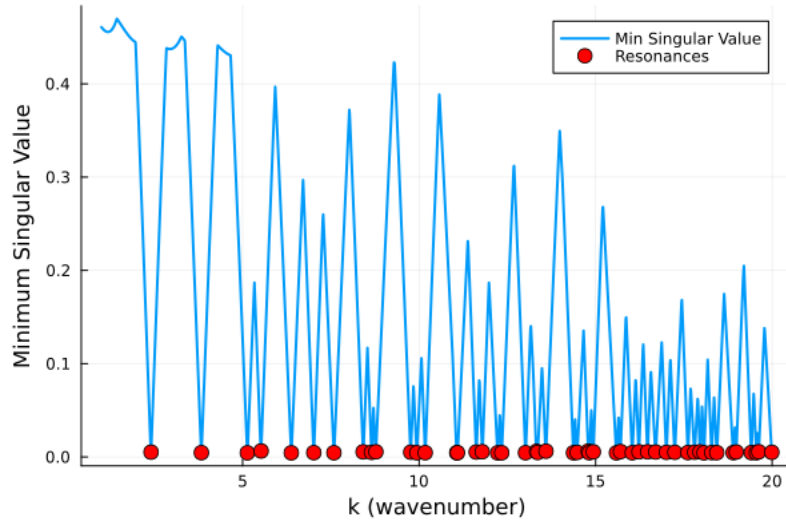


Figure 3: Evolution of minimum singular value for k up to 20 in a unit circle billiard

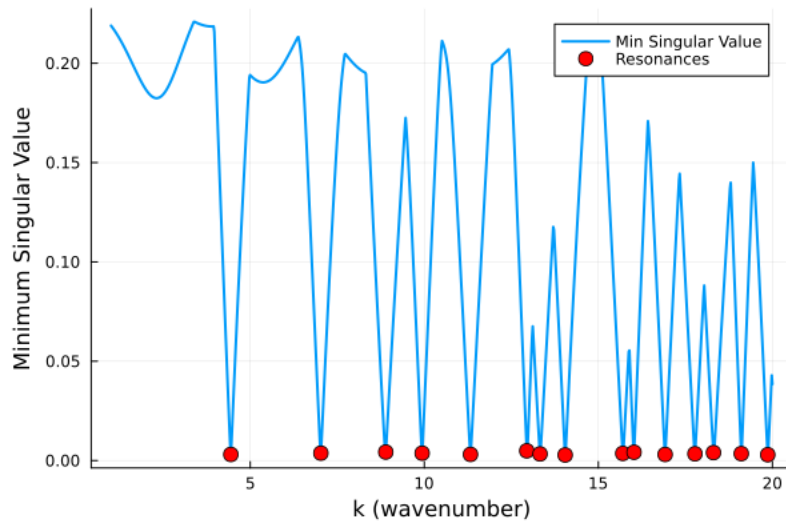


Figure 4: Evolution of minimum singular value for k up to 20 in a square billiard of side length 1

mode	circle	square
1	2.40417	4.44107
2	3.83114	7.02330
3	5.13556	8.88444
4	5.51938	9.93425
5	6.38012	11.32607
6	7.01570	12.95255
7	7.58763	13.32782
8	8.41703	14.04796
9	8.65358	15.70769
10	8.77139	16.03735

Table 1: First 10 resonant modes for the circle and square billiard approximated by our BEM

Circular billiard The problem of a circular billiard can be thought of as a particle with mass m being confined to an infinite circular well. As a system, we can imagine it as free space subjected to the circular potential

$$V(r) = \begin{cases} 0, & \text{if } r \leq a \\ \infty, & \text{if } r > a \end{cases}$$

To more easily work in this system, we redefine the time-independent Schrödinger equation

$$\left[-\frac{\hbar^2}{2\mu} \nabla^2 + V(r) \right] \psi(\mathbf{r}) = E\psi(\mathbf{r})$$

in terms of polar coordinates (r, θ) which yields

$$-\frac{\hbar^2}{2\mu} \left[\frac{\partial^2}{\partial r^2} + \frac{1}{r} \frac{\partial}{\partial r} + \frac{1}{r^2} \frac{\partial^2}{\partial \theta^2} \right] \psi(r, \theta) + V(r)\psi(r, \theta) = E\psi(r, \theta).$$

Using separation of variables, we decompose the wave-function into radial $R(r)$ and angular $\Theta(\theta)$ components, writing $\psi(r, \theta) = R(r)\Theta(\theta)$. From this, we can extract radial and angular equations

$$-\frac{\hbar^2}{2\mu} \left[\frac{d^2 R(r)}{dr^2} + \frac{1}{r} \frac{dR(r)}{dr} - \frac{l^2}{r^2} R(r) \right] + V(r)R(r) = ER(r)$$

and

$$\frac{d^2 \Theta(\theta)}{d\theta^2} = -l^2 \Theta(\theta)$$

respectively. Since $R(r) = 0$ outside the well due to the infinite potential, (radial) can be expressed as the Bessel equation

$$\frac{d^2 R(r)}{dr^2} + \frac{1}{r} \frac{dR(r)}{dr} + \left(k^2 - \frac{l^2}{r^2} \right) R(r) = 0$$

β_{ln}	$n = 1$	$n = 2$	$n = 3$	$n = 4$
$l = 0$	2.40483	5.52008	8.65373	11.7915
$l = 1$	3.83171	7.01559	10.1735	13.3237
$l = 2$	5.13562	8.41724	11.6198	14.7960
$l = 3$	6.38016	9.76102	13.0152	16.2235
$l = 4$	7.58834	11.0647	14.3725	17.6160

Table 2: Low order zeroes β_{ln} of the Bessel function.(ref)

where $k = \frac{\sqrt{2mE}}{\hbar}$ is the wavenumber. Such Bessel equations have two solutions: Bessel functions $J_l(kr)$ and Neumann functions $N_l(kr)$, both of order l . Since Neumann functions are divergent at $r = 0$, they are discarded [61]. As always, physically relevant values of k are defined by our chosen boundary conditions. Here, Dirichlet conditions amount to $R(r)|_{r=a} = 0$, so acceptable values of k are those which satisfy $J_l(ka) = 0$. In other words, the physical values of k are defined by

$$k_{ln} = \frac{\beta_{ln}}{a}$$

where β_{ln} is the n th root of the Bessel function of order l . Some examples of such roots are given in Table 1.

Square billiard We will again think of our problem as a particle of mass m in an infinite potential well [27, 29]. This time, we will take V to be the piecewise-defined "box" potential

$$V(x, y) = \begin{cases} 0, & 0 \leq x \leq L \text{ and } 0 \leq y \leq L \\ \infty, & x < 0 \text{ or } x > L \\ \infty, & y < 0 \text{ or } y > L \end{cases}$$

As before, restricting the problem to the inside of the well allows us to write (SE) as

$$-\frac{\hbar^2}{2m} \left(\frac{\partial^2 \psi(x, y)}{\partial x^2} + \frac{\partial^2 \psi(x, y)}{\partial y^2} \right) = E\psi(x, y).$$

Expressing the wave-function as $\psi(x, y) = X(x)Y(y)$ allows us to separate the variables along the Cartesian coordinates. This leads to 2 independent one-dimensional Schrödinger equations

$$-\frac{\hbar^2}{2m} \frac{d^2 X(x)}{dx^2} = \varepsilon_x X(x) \qquad -\frac{\hbar^2}{2m} \frac{d^2 Y(y)}{dy^2} = \varepsilon_y Y(y).$$

These equations have general solutions

$$X(x) = A_x \sin(k_x x) + B_x \cos(k_x x) \quad Y(y) = A_y \sin(k_y y) + B_y \cos(k_y y).$$

which are simplified to

$$X(x) = A_x \sin(k_x x) \quad Y(y) = A_y \sin(k_y y)$$

by applying Dirichlet boundary conditions, as we must have $\psi(0, y) = \psi(x, 0) = 0$. Now, we can partially reconstruct the wave function $\psi(x, y)$ as

$$\psi(x, y) = N \sin\left(\sqrt{\frac{2m\varepsilon_x}{\hbar^2}} x\right) \sin\left(\sqrt{\frac{2m\varepsilon_y}{\hbar^2}} y\right).$$

By further requiring $\psi(L, y) = \psi(x, L) = 0$, we find we must satisfy

$$N \sin\left(\sqrt{\frac{2m\varepsilon_x}{\hbar^2}} L\right) \sin\left(\sqrt{\frac{2m\varepsilon_y}{\hbar^2}} y\right) = 0 \quad N \sin\left(\sqrt{\frac{2m\varepsilon_x}{\hbar^2}} x\right) \sin\left(\sqrt{\frac{2m\varepsilon_y}{\hbar^2}} L\right) = 0$$

which is the case when

$$\sin\left(\sqrt{\frac{2m\varepsilon_x}{\hbar^2}} L\right) = 0 \quad \sin\left(\sqrt{\frac{2m\varepsilon_y}{\hbar^2}} L\right) = 0.$$

This is the case when $\sqrt{\frac{2m\varepsilon_x}{\hbar^2}} L = n_x \pi$ and $\sqrt{\frac{2m\varepsilon_y}{\hbar^2}} L = n_y \pi$ for integers n_x, n_y . This allows us to define acceptable values of E as

$$E_{n_x, n_y} = \frac{\hbar^2 \pi^2}{2mL^2} (n_x^2 + n_y^2)$$

and thus physical values of k as

$$k_{n_x, n_y} = \pi \sqrt{n_x^2 + n_y^2}.$$

The first 10 resonant frequencies of a square billiard with side length one are presented in Table 3. Repeated resonances have been omitted as they produce functionally identical results. However, we shall return to these at the end of this chapter when investigating the effects of symmetry.

Comparison Comparing the results of Tables 2 and 3 to our results, it's clear that the first resonant modes of these systems are well approximated by our implementation of the BEM. Preserving this accuracy as higher frequencies get closer together, as seen in Fig. 3, involves increasing the number of evaluation points in the

<i>modes</i>	(n_x, n_y)	$k = \pi\sqrt{n_x^2 + n_y^2}$
1	(1, 1)	4.44288
2	(2, 1)	7.02481
3	(2, 2)	8.88577
4	(3, 1)	9.93459
5	(3, 2)	11.32717
6	(4, 1)	12.95312
7	(3, 3)	13.32865
8	(4, 2)	14.04963
9	(4, 3)	15.70796
10	(5, 1)	16.01904

Table 3: First resonant frequencies of the square billiard with side length of 1

spectrum of k as well as increasing the number of boundary elements N .

4.2 Solutions to the Helmholtz equation

Equipped with our approximated modes, we can now define a set of solvable matrix equations corresponding to the physical solutions of the Helmholtz eigenproblem. In our implementation, these matrix equations are solved by computing the singular vectors for each resonant frequency. These values are then reintroduced into (21) as

$$\frac{\partial\psi}{\partial\mathbf{n}} = \sum_{n=1}^N w_n \phi(x_n). \quad (28)$$

Explicitly, $w_n \phi(x_n)$ describes the density of $\frac{\partial\psi}{\partial\mathbf{n}}$ at an associated node x_n . This is illustrated in Fig. 6, where we can see the evolution along $\partial\Omega$ of the real and imaginary components of $\frac{\partial\psi}{\partial\mathbf{n}}$ in blue and orange respectively, with its absolute value represented in green. This discretised boundary data can finally be reintroduced into the representation theorem (8) from Chapter 2, defining solutions to the Helmholtz equations on Ω as

$$\psi(x) = \sum_i G(x, r_i) \frac{\partial\psi}{\partial\mathbf{n}}(r_i) ds_y, \quad \forall x \in \Omega. \quad (29)$$

Here, our free-space Green's function will no longer display singularities as $\Omega \cap \partial\Omega = \emptyset$. We have used (29) to graph the first 6 resonant eigenmodes in Fig. 6. At a glance, these correspond nicely to Fig. 5; graphs with complete radial symmetry display constant functions while those which are subdivided by axes of symmetry, such as $k = 5.13556$, display accordingly sinusoidal functions. Comparing our results to those of Kaufman et al [39] in Fig. 7, it is clear to see that our implementation of the boundary element method has worked in approximating the resonant modes and wave function solutions of the Helmholtz equation.

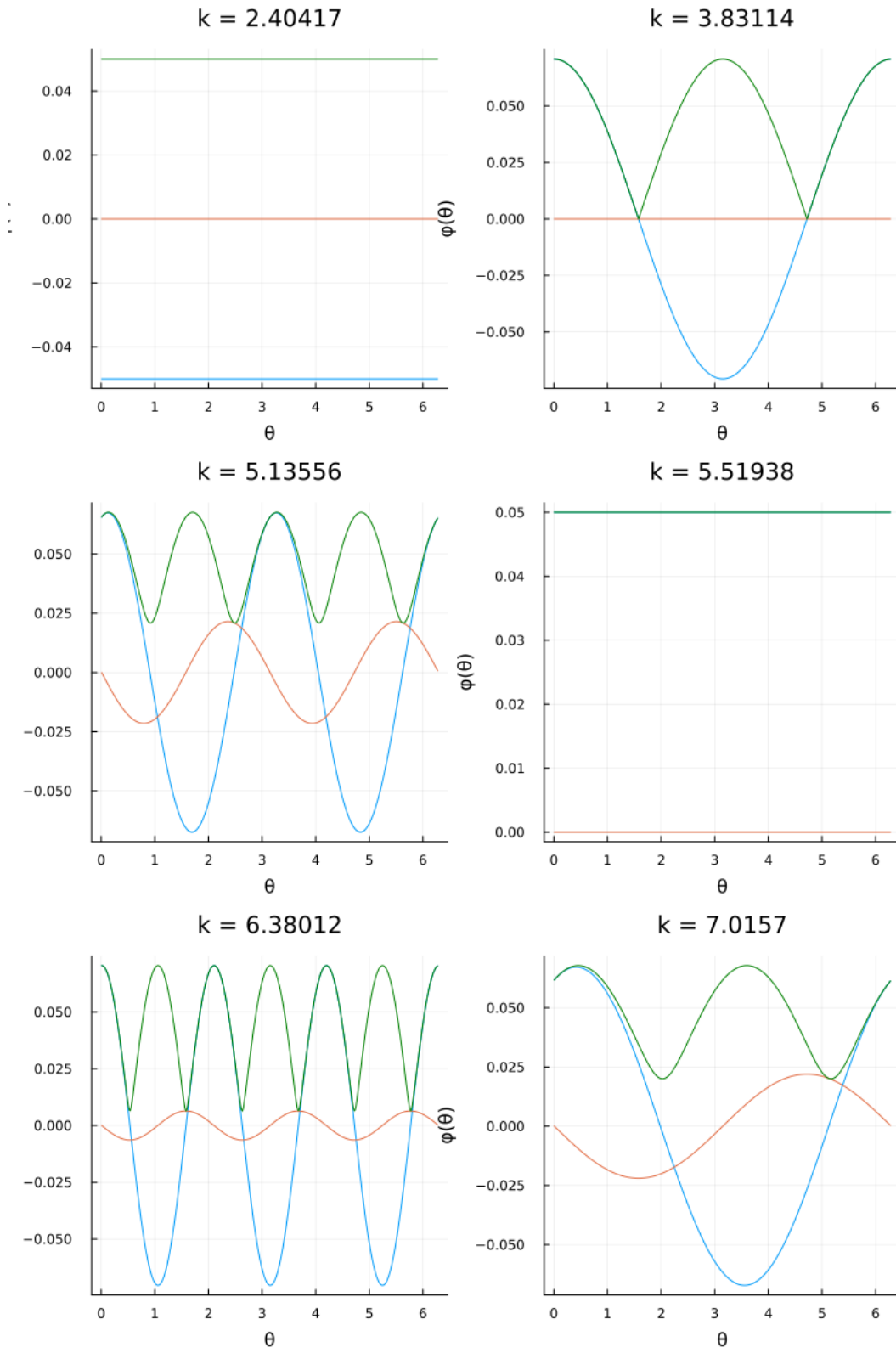


Figure 5: Boundary data of the circle billiard over a range of resonant k

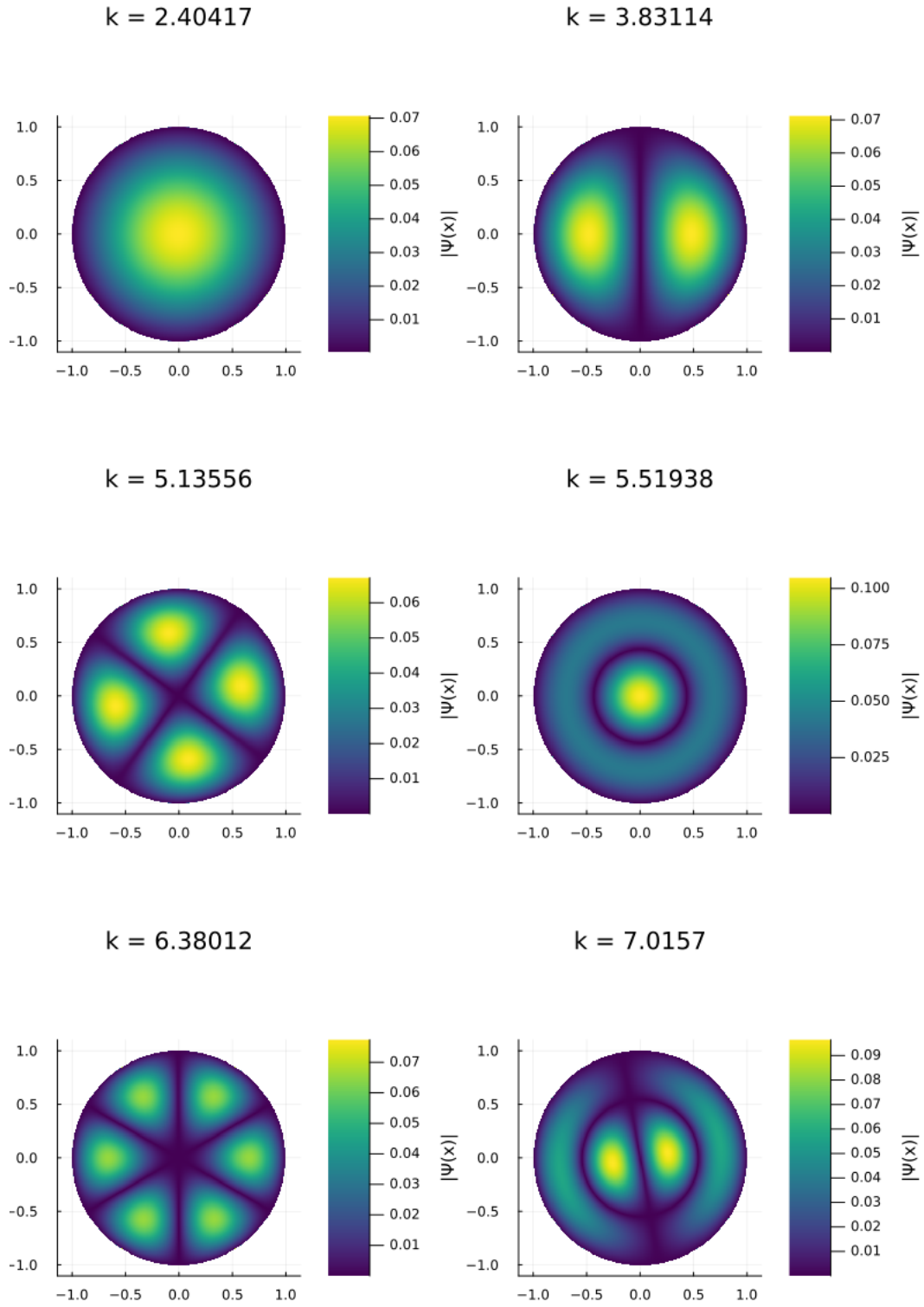
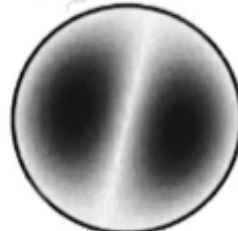


Figure 6: Wavefunction visualisation in the unit circle over a range of resonant k

$$k_1 = 2.4002$$



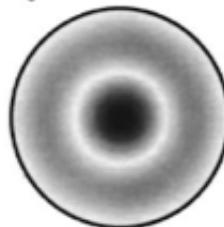
$$k_3 = 3.8226$$



$$k_5 = 5.1273$$



$$k_6 = 5.5099$$



$$k_7 = 6.3679$$



$$k_9 = 6.9997$$

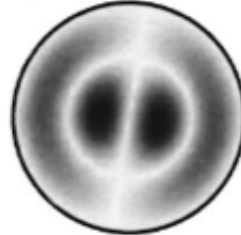


Figure 7: Results of Kaufman et al.

4.3 Symmetry and degenerate spectra

The dynamics of billiard systems, both classical and quantum, are strongly dictated by their symmetries. This can be seen in the fact that billiards with one axis of symmetry present solutions that are completely symmetric along this axis [49]. A simple example, illustrated in Fig. 8, is that of the cardioid billiard, which has one horizontal axis of symmetry. In the case where one or more axes of symmetry subdivide the billiard as in Fig. 6, we see that we could define a sub-billiard with the same Dirichlet boundary conditions, which has a spectrum that is approximately a subset of the larger billiard. One example is that of the quarter-circle [39]. In this case, even more insight into the original spectrum could be gained by applying Neumann boundary conditions to one or both of the axes of symmetry, which make up the straight sides of the quarter circle. Such systems are also successfully addressed by BEMs [13]. Whilst not rigorous, the benefit of this constructive approach is that it reveals how symmetry-induced degeneracies appear in the spectrum of the complete billiard system.

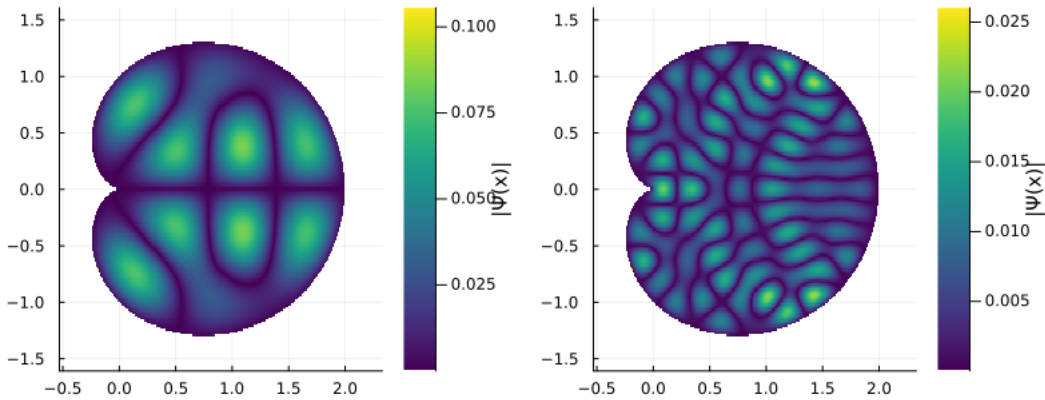


Figure 8: Solutions to the cardioid billiard at modes $k = 6.783$ and $k = 17.045$

Let's reconsider the example of the square billiard. We saw that solutions, energy levels, and eigenmodes of this system take the forms

$$\psi(x, y) = N \sin(n_x \pi x) \sin(n_y \pi y), \quad E_{n_x, n_y} = \frac{\hbar^2 \pi^2}{2mL^2} (n_x^2 + n_y^2), \quad k_{n_x, n_y} = \pi \sqrt{n_x^2 + n_y^2},$$

respectively. At a glance, we would expect the resulting solutions to form $n_y \times n_x$ grids over Ω as the sinusoidal functions propagate along the y and x axes, respectively. However, at closer inspection, we see that these expressions are left completely unchanged by switching the values of n_x, n_y , leading to degenerate solutions,

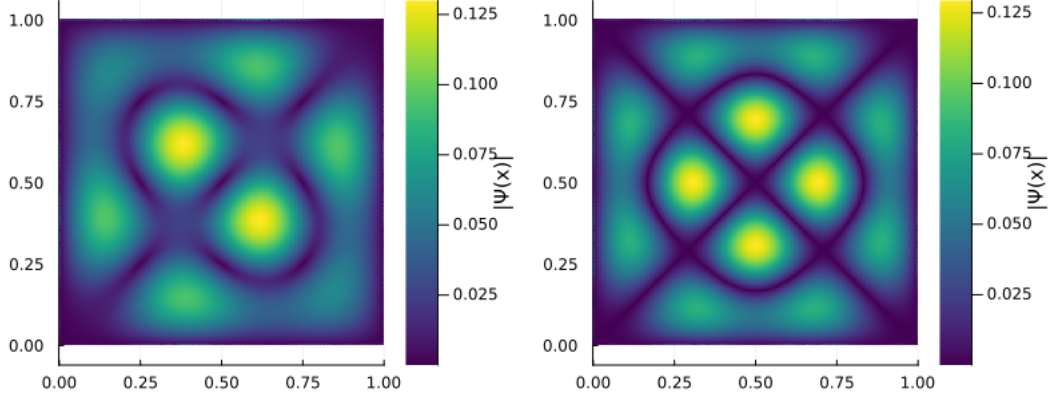


Figure 9: Degenerate square billiard solutions

energies, and eigenmodes. This is illustrated in Fig. 9, where the solutions at eigenmodes $k = 12.95312$ and $k = 16.01904$ appear as superpositions of our expected grids. This degeneracy is the result of the set of symmetries on the square, known as the dihedral group D_4 , comprised of reflections about midlines and diagonals, and rotations of $\frac{\pi}{2}, \pi, \frac{3\pi}{2}$ about the centre of the square. In the context of quantum mechanics, this means that the Hamiltonian of our system commutes with every element in D_4 as

$$[H, P] = 0, \quad \forall P \in D_4.$$

To explicitly show that this degeneracy is due to D_4 symmetries, we must simply consider the analogous system of a rectangle with sides of length 1 and $\sqrt{2}$, which breaks them. Repeating the calculations from the above section, we instead reach

$$\psi(x, y) = N \sin(n_x \pi x) \sin\left(\frac{n_y \pi y}{\sqrt{2}}\right), \quad E_{n_x, n_y} = \frac{\hbar^2 \pi^2}{2m} \left(n_x^2 + \frac{n_y^2}{2} \right), \quad k_{n_x, n_y} = \pi \sqrt{n_x^2 + \frac{n_y^2}{2}}.$$

Breaking D_4 symmetry by lengthening the square billiard into a rectangle leads to equations which are no longer degenerate. This implies that the spectrum too is non-degenerate, which is clear as

$$E_{2,1} \propto 4 + \frac{1}{2} = 4.5, \quad E_{1,2} \propto 1 + \frac{4}{2} = 3.$$

This is best illustrated by the fact that the solutions of rectangular billiards regain their expected grid forms as seen in Fig. 10.

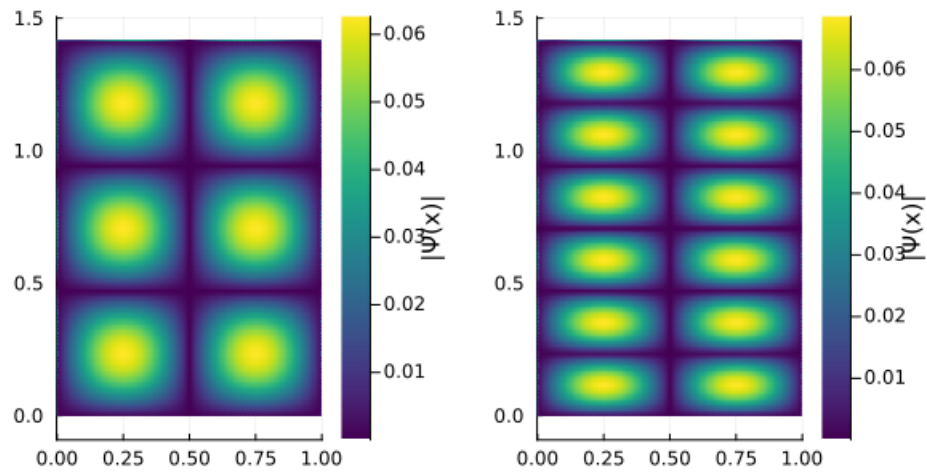


Figure 10: Non-degenerate rectangular billiard solutions

5 Spectral statistics

We are now equipped with a computational tool for approximating the spectrum of modes of quantum billiard systems with piecewise smooth boundaries $\partial\Omega$. From here, our aim shifts to investigating the semi-classical limits of these systems, seeing how the dynamics of classical billiards manifest in the quantum regime. After defining the notion of classical integrability and chaos, we consider Weyl's theorem and the notion of spectral unfolding. These steps are crucial if we seek to make meaningful comparisons between different billiard spectra. We then compute the mode spacing density distribution of the integrable rectangle billiard and the chaotic cardioid. Comparing these leads to the conclusion that while integrable systems follow a Poisson distribution, indicative of level attraction, the distributions of chaotic spectra instead show clear signs of level repulsion.

5.1 Liouville Integrability

Classical chaos is commonly referred to as a "loss of conserved quantities". Indeed, so-called "integrable" billiards are those which conserve n quantities for the n degrees of freedom that the Hamiltonian displays. To formalise this, we start by defining a dynamical billiard upon a $2n$ -dimensional phase space Ω which can be parametrised by canonical variables

$$(q_\mu, p_\mu). \quad (30)$$

As such, both the Hamiltonian H and functions F on Ω are defined as functions of (q_μ, p_μ) . In an attempt to determine the evolution of such functions F , let us consider

$$\dot{F} = \frac{dF}{dt} = \sum_{\mu=1}^n \left(\frac{\partial F}{\partial q_\mu} \dot{q}_\mu + \frac{\partial F}{\partial p_\mu} \dot{p}_\mu \right). \quad (31)$$

It's clear from the Hamilton equations that the RHS of this expression can be expressed as the Poisson bracket of F and H

$$\{F, H\} = \sum_{\mu=1}^n \left(\frac{\partial F}{\partial q_\mu} \frac{\partial H}{\partial p_\mu} - \frac{\partial F}{\partial p_\mu} \frac{\partial H}{\partial q_\mu} \right). \quad (32)$$

This leads us to describe (31) as $\dot{F} = \{F, H\}$, which describes the evolution on Ω of any function F . We can infer that any function F satisfying $\{F, H\} = 0$ is conserved. In any system, the first conserved quantity is the Hamiltonian, as $\{H, H\} = 0$ by definition. An $2n$ -dimensional system is called *Liouville integrable* if it has n -independent conserved quantities in involution [59, 36]

$$\{F_\mu, F_\nu\} = 0, \quad \mu, \nu = 1, \dots, n. \quad (33)$$

Such systems have the distinct advantage of being completely solvable by Liouville’s theorem, which states that the equations of motion of a Liouville integrable system can be solved by quadratures. In other terms, this means that there always exists a canonical transformation of variables which leads to an equation of motion coinciding with a conserved quantity. As seen in the previous chapter, these were polar coordinates in the case of the circle billiard, and Cartesian coordinates in the case of the square and rectangle billiards. These billiards and their dynamics are known as integrable.

Accordingly, billiards which do not display this feature are known as chaotic [10]. The relative ”amount” of chaos varies depending on the particular boundary, with the Bunimovich stadium [68], cardioid [62], and Sinai billiards displaying strong chaos. The transition between integrability and complete chaos is nicely illustrated by the smooth transition between the circle and cardioid billiard in [62].

5.2 Weyl’s law and spectral unfolding

The distribution and density of energy levels are geometry-driven, defined almost exclusively by the size and shape of the billiard boundary. This manifests as systematic trends in energy level and mode density, such as larger billiards having modes more closely spaced, for example. This dependence obscures small-scale fluctuations caused by chaotic or integrable behaviours, and is quantified by Weyl’s theorem [9, 2] for 2-dimensional bounded Helmholtz eigenproblems. This theorem states that the energy spectrum of our class of billiard systems becomes denser by a counting function $N(E)$. This function is defined as

$$N(E) \approx \frac{A}{4\pi}E - \frac{L}{4\pi}\sqrt{E}, \quad (34)$$

and describes the average number of energy levels beneath a given threshold E for given area A and boundary length L of the billiard. This function can be easily converted to describe eigenmode density by taking $E = k^2$. We compare Weyl’s prediction to the results from our implementation for the rectangle and cardioid billiards in Figs. 11 and 12. We pick the rectangle as our integrable billiard as it produces a non-degenerate spectrum, as shown in Section 4.3, allowing us to use our implementation. We pick the cardioid as our chaotic billiard as it is maximally chaotic, making any divergence from the statistics of integrable billiards more stark. It’s clear from these figures that our method only follows Weyl’s prediction for the first 100 or so resonant modes, so we select this interval for further investigation.

The counting function contains the geometric contributions of billiard boundaries to the density of their energy spectrum. As such, it can be used to remove such contributions, allowing for comparisons to be drawn between the density spacing spectra of different billiards. This process, known as spectral unfolding

[32], first involves defining a new spectrum using Weyl’s theorem

$$u_i = N(k_i). \quad (35)$$

This process effectively normalises the spectrum to a uniform baseline, removing the geometry-driven increase in density. This new spectrum has an average spacing of 1 between energy levels. We then define our spacing distribution as

$$s_i = x_{i+1} - x_i. \quad (36)$$

This provides a statistically comparable baseline that overtly displays the integrable or chaotic behaviours of the billiard system from which it is drawn.

5.3 Integrable and chaotic systems

Having developed the numerical conditioning required to make comparisons between the eigenmode spectra of various billiards, we can now use our implementation of the BEM to investigate the effects of classically integrable and chaotic boundaries. As examples, we have taken the rectangle and cardioid billiards, evaluated in the trusted window of modes defined above.

In Fig. 13, the rectangle billiard is shown to display signs of level attraction, with the likelihood of larger spacings decreasing sharply. This closely follows the Poisson [12] distribution

$$P(s) = e^{-s}, \quad (37)$$

which has been overlaid in green for the sake of comparison. The same graph is produced for the cardioid billiard in Fig. 14. In this case, we see that the signs of level attraction have eased, giving way to level repulsion, as the likelihood of finding very small spacings decreases.

This behaviour extends to all classically integrable and chaotic billiards [31, 67], with the former following the Poisson distribution (37) and the latter diverging to another distribution as more resonant modes are considered. It would seem that the quantum property of resonant mode spacing distribution is directly impacted by the chaotic behaviour of their classical analogues.

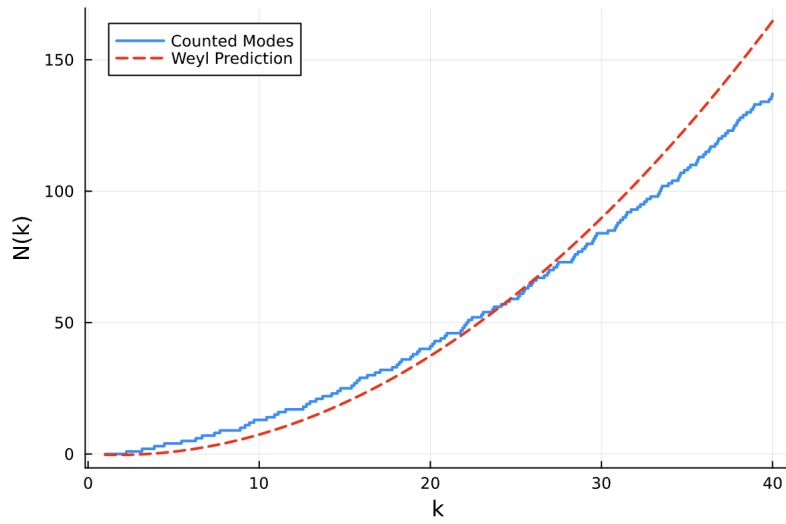


Figure 11: Comparison of the cumulative sum of detected resonant modes of the rectangle billiard to the Weyl prediction

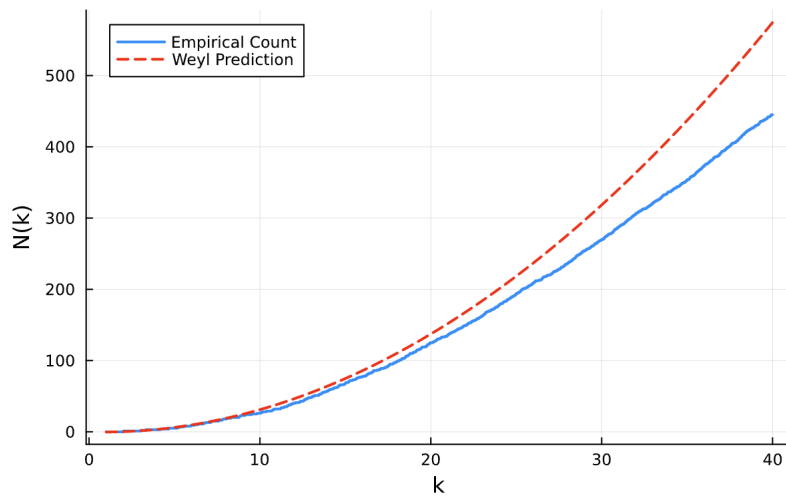


Figure 12: Comparison of the cumulative sum of detected resonant modes of the cardioid billiard to the Weyl prediction

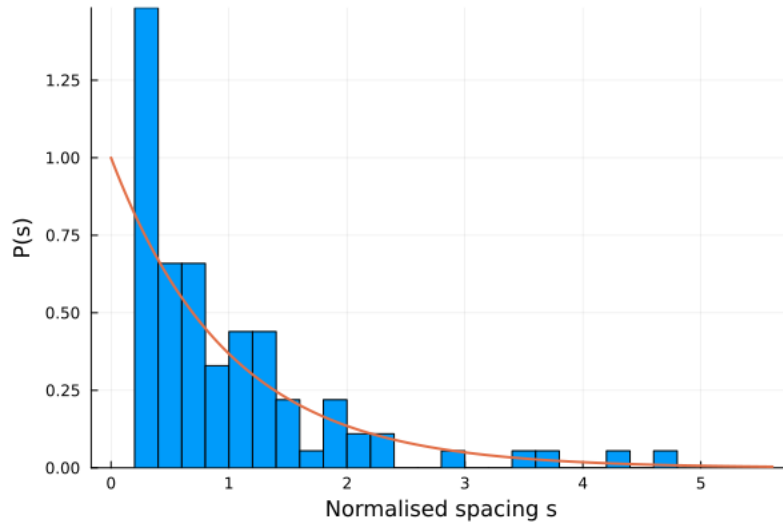


Figure 13: Normalised resonant mode density distribution of the rectangle billiard

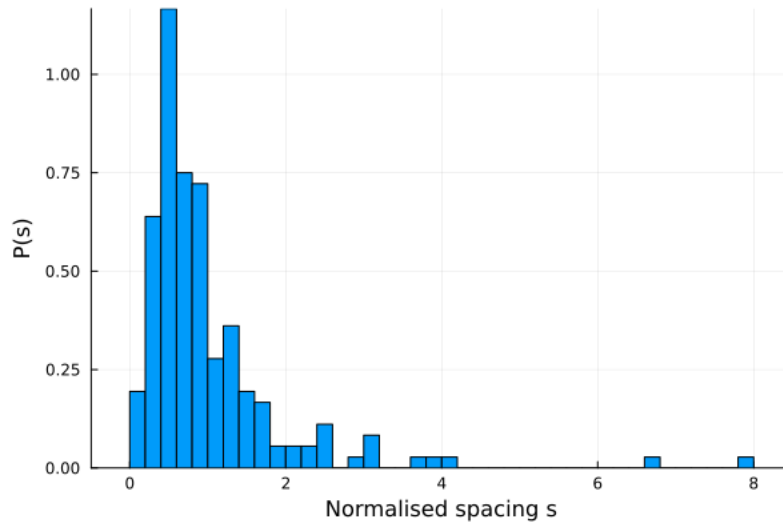


Figure 14: Normalised resonant mode density distribution of the cardioid billiard

6 Random Matrix Theory

The level (both resonant modes and energies) spacing distribution that emerges from chaotic quantum billiard systems was conjectured by Bohigas, Giannoni, and Schmit to be best described by the Wigner-Dyson distributions [16], which emerged from attempts to investigate the spectra of complex atomic nuclei. This distribution corresponds to the spectrum of eigenvalues generated by ensembles of matrices with entries chosen from specific probability distributions. The study of the properties of such matrices and the probability distributions they generate is known as Random Matrix Theory (RMT). Here, we investigate the basics of RMT, constructing the Wigner-Dyson distribution in its many forms. We then compare these distributions to our results from Chapter 5 to verify the since-confirmed BGS conjecture, describing the energy spacing spectrum of chaotic quantum billiards with the Gaussian Orthogonal Ensemble.

6.1 Constructing Wigner-Dyson distributions

Our study of quantum billiards has led us to describe a real positive spectrum of eigenmodes; this is mirrored by the spectrum of hermitian matrices, which we shall focus on from now. Let's consider an example hermitian matrix with entries taken from a Gaussian distribution with mean 0 and variance σ [21]. A 2x2 matrix with these properties takes the form

$$\hat{H} = \begin{bmatrix} \lambda_1 & \frac{\lambda_3}{\sqrt{2}} \\ \frac{\lambda_3^*}{\sqrt{2}} & \lambda_2 \end{bmatrix} \quad (38)$$

where the off-diagonal terms are multiplied by a factor $\frac{1}{\sqrt{2}}$ as per convention. We will elucidate the reasoning for this later. If the entries of \hat{H} are real and thus the off-diagonal entries satisfy $\lambda_3 = \lambda_3^*$, it is said that the 2-level system displays "time-reversal symmetry". If this is not the case, then we take the real and imaginary parts of each entry to be separate variables, taking each from the above Gaussian distribution. In the case of time-reversal symmetry, we can define [21] the energy spacing statistics of $\omega = E_1 - E_2$ as

$$P(\omega) = \frac{1}{(2\pi)^{3/2}\sigma^3} \int d\lambda_1 \int d\lambda_2 \int d\lambda_3 \delta\left(\sqrt{(\lambda_1 - \lambda_2)^2 + 2\lambda_3^2} - \omega\right) \exp\left[-\frac{\lambda_1^2 + \lambda_2^2 + \lambda_3^2}{2\sigma^2}\right].$$

For ease, we convert the integral over λ_1 into a Gaussian integral by the change of variables $\lambda_2 = \lambda_1 + \sqrt{2}\chi$, which gives us

$$P(\omega) = \frac{1}{2\pi\sigma^2} \int \int d\chi d\lambda_3 \delta\left(\sqrt{2\chi^2 + 2\lambda_3^2} - \omega\right) \exp\left[-\frac{\chi^2 + \lambda_3^2}{2\sigma^2}\right].$$

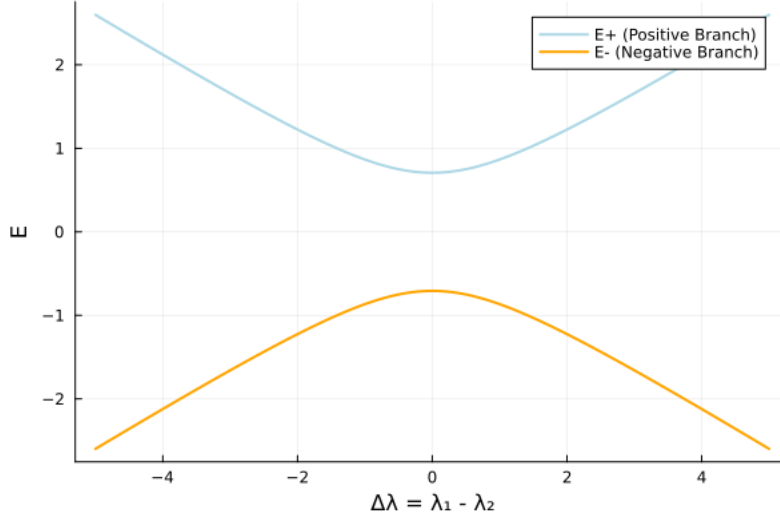


Figure 15: Energy level repulsion in a 2-dimensional system

The remaining integrals are computed by a change of coordinates of $\lambda_3 = r \cos(x)$ and $\chi = r \sin(x)$. This yields the energy spacing probability distribution

$$P(\omega) = \frac{\omega}{2\sigma^2} \exp \left[-\frac{\omega^2}{4\sigma^2} \right].$$

If time-reversal symmetry is broken, an equivalent calculation would lead to

$$P(\omega) = \frac{\omega^2}{2\sqrt{\pi}(\sigma^2)^{3/2}} \exp \left[-\frac{\omega^2}{4\sigma^2} \right].$$

Normalising both cases and setting the mean energy spacing gives

$$P_1(\omega) = \frac{\pi}{2} \omega \exp \left[-\frac{\pi}{4} \omega^2 \right], \quad P_2(\omega) = \frac{32}{\pi^2} \omega^2 \exp \left[-4\pi \omega^2 \right]. \quad (39)$$

Both distributions display the same key features. The first is that they decay as Gaussians as ω increases. The second, more interesting, feature is that for small spacing $\omega \rightarrow 0$, $P(\omega)$ also tends to 0. This is a clear sign of level repulsion. These distributions can be generalised to

$$P(\omega) = N_\gamma \omega^\gamma \exp \left[-M_\gamma \omega^2 \right], \quad (40)$$

known as the *Wigner surmise*, where N_γ and M_γ are normalisation constants and γ is the variance. In this case, $\gamma = 1$ indicates the system has time-reversal symmetry and $\gamma = 2$ indicates that it does not.

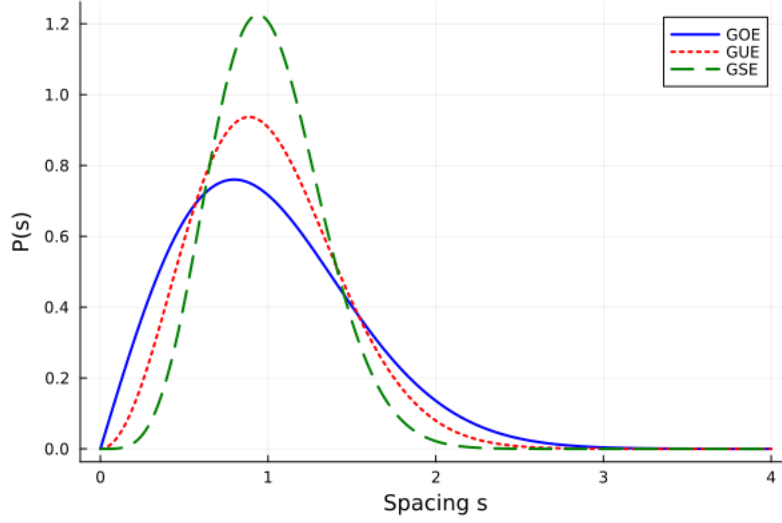


Figure 16: Illustration of the Wigner-Dyson Distributions

We can generalise this idea to matrices of higher dimensions by defining an ensemble of matrices with entries taken from the Gaussian distribution as in (38). This leads to the distribution of these random matrices given by

$$P(\hat{H}) \propto \exp \left[-\frac{\gamma}{2p^2} \sum_{i,j} H_{ij} H_{ji}^* \right] \equiv \exp \left[-\frac{\gamma}{2p^2} \sum_{i,j} H_{ij} H_{ji} \right], \quad (41)$$

where p is the energy scale which is analogous to the variance of the distribution; if p is large, then the eigenvalue spectrum will be more spread out and vice-versa. The factor of $\frac{1}{\sqrt{2}}$ shows its importance in (41), as without it the Hamiltonian could not be expressed by the distribution. As in the Wigner surmise, $\gamma = 1$ indicates real valued matrices with time reversal symmetry where $\hat{H}_{ij} = \hat{H}_{ji}$, and defines the Gaussian Orthogonal Ensemble (GOE). Similarly, $\gamma = 2$ refers to systems without time-reversal symmetry where $\hat{H}_{ij} = \hat{H}_{ji}^*$, the set of which is known as the Gaussian Unitary Ensemble (GUE). Furthermore, we can define the Gaussian Symplectic Ensemble (GSE) by taking $\gamma = 4$. This is the ensemble of symplectic matrices M satisfying $M\Omega M^{-1} = \Omega$ where Ω is the standard symplectic matrix [30]. The level spacing statistics of these ensembles are known as the Wigner-Dyson distributions [43] and do not have closed analytic forms [21, 41]. Fortunately, they are close enough to the Wigner surmise for all practical purposes. These distributions, as defined by the Wigner surmise, are represented in Fig. 16.

6.2 Comparison to the spectra of chaotic systems

On the surface, the Wigner-Dyson distributions would seem like good candidates to describe the level spacing density functions of chaotic spectra, as we observe similar level repulsion, illustrated for the 2-dimensional system in Fig. 15. Indeed, from Fig. 17, we see that even the comparatively low-energy spectrum produced by our BEM implementation tends towards the GOE [16], shown in red. Furthermore, the Wigner-Dyson distributions appear in other dynamical quantum systems with classical analogues such as the kicked rotor, which displays the GUE [54]. This behaviour is only exacerbated at higher energies [16, 30, 21]. In the case of mixed classical chaotic behaviour, the Poisson and Wigner-Dyson distributions are generalised by the Porter-Thomas distributions [39, 50].

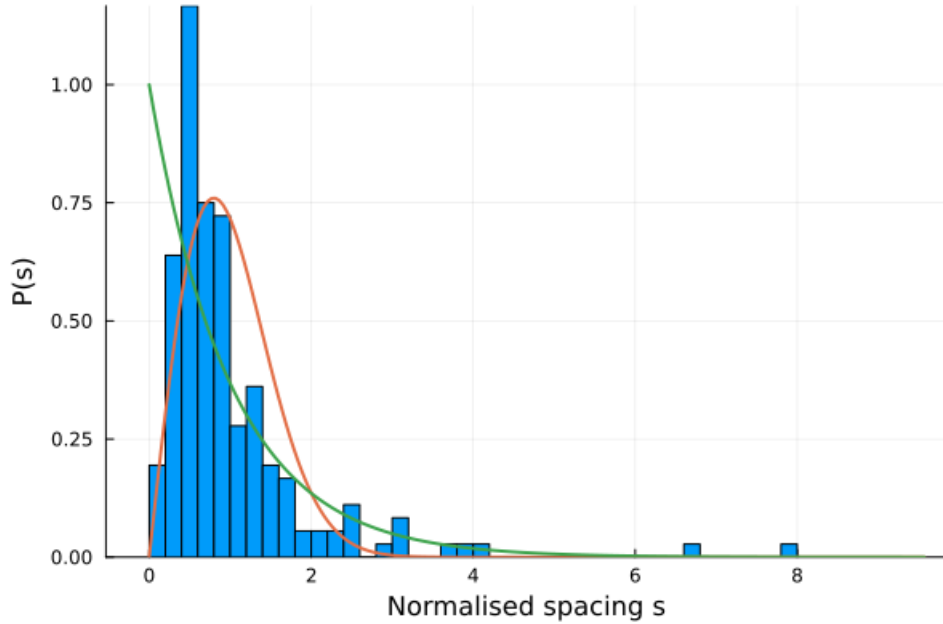


Figure 17: Comparison between the level-spacing of normalised chaotic spectrum, the Poisson distribution (green), and the Gaussian Orthogonal Ensemble (red)

7 Conclusion and Outlook

We began with the question *"How does chaos in classical billiard systems manifest in the semi-classical limit?"*. To answer this question, we explored boundary element methods as computationally efficient methods of addressing quantum billiard systems with arbitrary boundaries. We did so with the aim of creating our own implementation of a BEM in the Julia programming language.

In Chapter 2, we derived Green's representation theorem and showed how it could be used in conjunction with known boundary conditions to produce boundary integral equations. These equations, which produce data along the boundary, were then assessed for numerical stability and solved using discretisation methods. We explored the Nyström and Bubnov-Galerkin methods but concluded that we would use the former for our own BEM implementation in Chapter 3. In Chapter 4, we discussed how eigenmode and wave function solutions could be drawn from our findings, and compared the results from our implementation against analytical solutions and well-known examples from the literature. We also did some mild spectral analysis, commenting on the role of billiard symmetry in the degeneracy of eigenmode spectra.

Content with the accuracy of our implementation, we turned our attention back to our central question in the second half of this thesis. In Chapter 5, we discussed the notion of classical chaos and integrability to determine which billiards should be pitted against one another. We then decided that energy spacing statistics would be our choice of comparison. Using Weyl's energy level density prediction, we removed the geometry dependence of our energy spectra, allowing small-scale chaotic fluctuations to emerge. Equipped with this metric, we investigated the energy spacing distributions of classically integrable and chaotic billiard systems, respectively. We found that while the former followed a Poisson distribution, the latter showed signs of level repulsion and displayed a completely different distribution. This distribution is known as the Gaussian Orthogonal Ensemble, one of the Wigner-Dyson distributions which arise from Random Matrix Theory. In Chapter 6, we explored the basics of RMT and built an understanding of the Wigner-Dyson distributions. We concluded by confirming that, unlike classically integrable systems, the level spacing distribution of chaotic billiards follows the Gaussian Orthogonal Ensemble.

A natural continuation of this thesis is to explore the eigenvector statistics [6] and chaotic eigenfunctions [7] which arise in quantum billiard systems, deepening our understanding of the effects of classical chaos. Refinements to our BEM implementation could be made, as well as exploring alternative approximation methods such as expansion methods [39] and the use of machine learning techniques [34]. Such refinements would allow us to investigate high-energy effects such as scarring and ergodicity [11, 5].

As mentioned in Chapter 1, the practical applications of research into quantum chaos are numerous, from

quantum computation [45, 50] to laser technology optimisation [67]. The ideas presented in RMT are even more far-reaching. Not only can they be expanded to many-bodied quantum systems, but to pure mathematics [66], biology [47], and beyond. Altogether, this thesis provides an introduction to the very exciting intertwined fields of quantum chaos and random matrix theory.

A Boundary Element Method code

Here we detail the main functions of our BEM implementation. These are the same for any billiard, but we shall provide the details of the rectangle billiard as an example for computations to be replicated.

```
# We have used the dependencies
using LinearAlgebra
using SpecialFunctions
using Plots
using Statistics

# Boundary dimensions
const Lx = 1.0
const Ly = sqrt(2)
const L_total = 2*(Lx + Ly) # total boundary length

# Boundary parameterisation (take s in [0, L_total) to parametrise
# entire boundary
function rect_boundary(s::Float64)
    if s < Lx
        # Bottom edge: from (0,0) to (Lx,0)
        return [s, 0.0]
    elseif s < Lx + Ly
        # Right edge: from (Lx,0) to (Lx,Ly)
        s2 = s - Lx
        return [Lx, s2]
    elseif s < 2*Lx + Ly
        # Top edge: from (Lx,Ly) to (0,Ly)
        s3 = s - (Lx + Ly)
        return [Lx - s3, Ly]
    else
        # Left edge: from (0,Ly) to (0,0)
        s4 = s - (2*Lx + Ly)
        return [0.0, Ly - s4]
```

```

        end
    end
end

# Tangent vectors (constant along each edge)
function rect_derivative(s::Float64)
    if s < Lx
        return [1.0, 0.0]
    elseif s < Lx + Ly
        return [0.0, 1.0]
    elseif s < 2*Lx + Ly
        return [-1.0, 0.0]
    else
        return [0.0, -1.0]
    end
end

# Outward normal (again constant on each edge)
function outward_normal(s::Float64)
    if s < Lx
        return [0.0, -1.0]      # bottom edge: interior is above
    elseif s < Lx + Ly
        return [1.0, 0.0]      # right edge: interior is left
    elseif s < 2*Lx + Ly
        return [0.0, 1.0]      # top edge: interior is below
    else
        return [-1.0, 0.0]     # left edge: interior is right
    end
end

# Quadrature weights
function quadrature_weights_rect(s_vals)
    N = length(s_vals)
    ds = L_total / N

```

```

        return fill(ds, N)
end

# Kernel function
function kernel(x::Vector{Float64}, n::Vector{Float64}, y::Vector{Float64}, k::Float64)
    rxy = norm(x - y)
    if rxy < 1e-8
        return -0.5 # take jump term in case of small separation
    else
        return (im * k / 4) * hankelh1(1, k * rxy) * dot(x - y, n) / rxy
    end
end

# BEM matrix
function build_BEM_matrix(k::Float64, N::Int)
    # Create a set of quadrature points along the boundary
    s_vals = collect(range(0, stop=L_total, length=N+1))[1:end-1] # avoid duplicating the endpoint
    xs = [rect_boundary(s) for s in s_vals] # Boundary point locations
    ns = [outward_normal(s) for s in s_vals] # Outward normals
    w = quadrature_weights_rect(s_vals) # Quadrature weights

    A = zeros(ComplexF64, N, N)
    # Assemble the BEM matrix using the Nyström method:
    for i in 1:N
        for j in 1:N
            A[i, j] = (i == j ? -0.5 : 0.0) + w[j] * kernel(xs[i], ns[i], xs[j], k)
        end
    end
    return A, s_vals, xs, ns, w
end

# Resonance detection
function find_resonances(N::Int, kmin::Float64, kmax::Float64, nk::Int)

```



```

ks = collect(range(kmin, kmax, length=nk))

smin = [abs(minimum(svdvals(build_BEM_matrix(k, N)[1]))) for k in ks]

resonant_indices = Int[]

for i in 2:length(smin)-1
    if smin[i] < smin[i-1] && smin[i] < smin[i+1] && smin[i] < 0.1
        # take only minima
        push!(resonant_indices, i)
    end
end

resonant_k = ks[resonant_indices]

return ks, smin, resonant_k
end

# At this point, we have approximated the resonant frequencies within a
# range of k. To recover the boundary data and visualise a solution at a
# given resonant k, run:

function compute_phi(k::Float64, N::Int)
    A, s_vals, xs, ns, w = build_BEM_matrix(k, N)
    S = svd(A)
    phi = S.V[:, end]      # Extract the right singular vector associated with the minimal singular value
    return phi, s_vals, xs, ns, w
end

function potential_at_point(x::Vector{Float64}, phi::Vector{ComplexF64},
                           xs::Vector{Vector{Float64}}, ns::Vector{Vector{Float64}},
                           w::Vector{Float64}, k::Float64)

    u = 0.0 + 0im
    N = length(xs)
    for j in 1:N
        u += phi[j] * w[j] * kernel(x, ns[j], xs[j], k)
    end
    return u
end

```

```

function heatmap_solution(k::Float64, N::Int, Nx::Int, Ny::Int)

    # Run BEM
    phi, s_vals, xs, ns, w = compute_phi(k, N)

    # Define a grid inside the rectangle (x in [0, Lx], y in [0, Ly])
    x_range = range(0, Lx, length=Nx)
    y_range = range(0, Ly, length=Ny)
    U = zeros(ComplexF64, Ny, Nx)

    # Evaluate wave function u(x) at each grid point.
    for (i, x_val) in enumerate(x_range)
        for (j, y_val) in enumerate(y_range)
            pt = [x_val, y_val]
            U[j, i] = potential_at_point(pt, phi, xs, ns, w, k)
        end
    end

    # Plot heatmap of the magnitude |u|
    heatmap(x_range, y_range, abs.(U), xlabel="x", ylabel="y",
            colorbar_title="|u|")
end

```

B Spectral Analysis code

Once we have determined the spectrum as above, we can visualise the counting function compared to the Weyl prediction and the normalised spacing distribution with:

```
# Weyl prediction
function weyl_prediction(k::Float64, area::Float64, perimeter::Float64)
    return (area / (4pi)) * k^2 - (perimeter / (4pi)) * k
end

# Comparison of BEM to Weyl prediction
function Weyl_comparison(N::Int, kmin::Float64,
                        kmax::Float64, nk::Int, area::Float64,
                        perimeter::Float64)

    ks, smin, resonant_k = find_resonances(N, kmin, kmax, nk)

    println("Detected resonant k values:")
    for k_val in resonant_k
        println("  k = $(round(k_val, digits=4))")
    end

    # Cumulative count of BEM modes
    mode_count = [sum(rk -> rk <= k, resonant_k) for k in ks]

    # Weyl's prediction
    weyl_N = [weyl_prediction(k, area, perimeter) for k in ks]

    p = plot(ks, mode_count, seriestype=:steppre, lw=2, label="Counted Modes",
            xlabel="k", ylabel="N(k)",
            plot!(p, ks, weyl_N, lw=2, ls=:dash, label="Weyl Prediction", linecolor=:red)
    display(p)
end
```

```

# Rescale eigenmodes
function rescale_eigenmodes(eigenmodes::Vector{Float64})
    spacings = diff(eigenmodes)
    mean_spacing = mean(spacings)
    unfolded = (eigenmodes .- eigenmodes[1]) ./ mean_spacing
    return unfolded
end

function analyse_resonances(k_resonant::AbstractVector)

    unfolded_k = rescale_eigenmodes(k_resonant)

    p = histogram(spacing_unfolded, bins=30, xlabel="Unfolded spacing s", ylabel="P(s)",
        legend=false, normalize=:pdf)

    # Can also overlay significant distributions
    # s_vals = range(0, stop=maximum(spacings)*1.2, length=200)
    # p_GOE = (pi/2) .* s_vals .* exp.(- (pi/4) .* s_vals.^2)
    # p_Poisson = exp.(-s_vals)

    # plot!(p, s_vals, p_GOE, lw=2, label="GOE: (pi/2) s exp(- (pi/4) s^2)")
    # plot!(p, s_vals, p_Poisson, lw=2, label="Poisson: exp(-s)")

    display(p)
end

```

References

- [1] John F Ahner. “Integral equations and the interior Dirichlet potential problem”. In: *Journal of Approximation Theory* 22.4 (1978), pp. 331–339.
- [2] Wolfgang Arendt et al. “Weyl’s law: Spectral properties of the Laplacian in mathematics and physics”. In: *Mathematical analysis of evolution, information, and complexity* (2009), pp. 1–71.
- [3] Kendall Atkinson and Alex Bogomolny. “The discrete Galerkin method for integral equations”. In: *Mathematics of computation* 48.178 (1987), pp. 595–616.
- [4] Kendall E Atkinson. “The numerical solution of boundary integral equations”. In: *Institute of mathematics and its applications conference series*. Vol. 63. Oxford University Press. 1997, pp. 223–260.
- [5] A Bäcker, R Schubert, and P Stifter. “Rate of quantum ergodicity in Euclidean billiards”. In: *Physical Review E* 57.5 (1998), p. 5425.
- [6] Arnd Bäcker. “Numerical aspects of eigenvalue and eigenfunction computations for chaotic quantum systems”. In: *The mathematical aspects of quantum maps*. Springer, 2003, pp. 91–144.
- [7] Arnd Bäcker and Roman Schubert. “Chaotic eigenfunctions in momentum space”. In: *Journal of Physics A: Mathematical and General* 32.26 (1999), p. 4795.
- [8] Péter Bálint et al. “What mathematical billiards teach us about statistical physics?” In: *arXiv preprint arXiv:2009.06284* (2020).
- [9] Nathanaël Berestycki and Mo Dick Wong. “Weyl’s law in Liouville quantum gravity”. In: *arXiv preprint arXiv:2307.05407* (2023).
- [10] Michael V Berry. “Regularity and chaos in classical mechanics, illustrated by three deformations of a circular billiard”. In: *European Journal of Physics* 2.2 (1981), p. 91.
- [11] Michael Victor Berry. “Quantum scars of classical closed orbits in phase space”. In: *Proceedings of the Royal Society of London. A. Mathematical and Physical Sciences* 423.1864 (1989), pp. 219–231.
- [12] Michael Victor Berry and Michael Tabor. “Level clustering in the regular spectrum”. In: *Proceedings of the Royal Society of London. A. Mathematical and Physical Sciences* 356.1686 (1977), pp. 375–394.
- [13] Timo Betcke, Erik Burman, and Matthew W Scroggs. “Boundary element methods with weakly imposed boundary conditions”. In: *SIAM Journal on Scientific Computing* 41.3 (2019), A1357–A1384.
- [14] Jeff Bezanson et al. “Julia: A fresh approach to numerical computing”. In: *SIAM Review* 59.1 (2017), pp. 65–98. DOI: 10.1137/141000671. URL: <https://epubs.siam.org/doi/10.1137/141000671>.
- [15] Carlo Bianca. “On the mathematical transport theory in microporous media: The billiard approach”. In: *Nonlinear Analysis: Hybrid Systems* 4.4 (2010), pp. 699–735.

- [16] O Bohigas, MJ Giannoni, and C Schmit. “Spectral properties of the Laplacian and random matrix theories”. In: *Journal de Physique Lettres* 45.21 (1984), pp. 1015–1022.
- [17] Michael Carley. “Numerical quadratures for singular and hypersingular integrals in boundary element methods”. In: *SIAM journal on scientific computing* 29.3 (2007), pp. 1207–1216.
- [18] David J Chappell and Gregor Tanner. “A boundary integral formalism for stochastic ray tracing in billiards”. In: *Chaos: An Interdisciplinary Journal of Nonlinear Science* 24.4 (2014).
- [19] Giulio Ciruolo. “A radiation condition for the 2-D Helmholtz equation in stratified media”. In: *Communications in Partial Differential Equations* 34.12 (2009), pp. 1592–1606.
- [20] David Colton and Rainer Kress. *Integral equation methods in scattering theory*. JOHN WILEY and SONS, 1983. URL: <https://api.semanticscholar.org/CorpusID:118224704>.
- [21] Luca D’Alessio et al. “From quantum chaos and eigenstate thermalization to statistical mechanics and thermodynamics”. In: *Advances in Physics* 65.3 (2016), pp. 239–362.
- [22] Brian Davies. *Integral transforms and their applications*. Vol. 41. Springer Science & Business Media, 2002.
- [23] Trevor W Dawson. “On the singularity of the axially symmetric Helmholtz Green’s function, with application to BEM”. In: *Applied mathematical modelling* 19.10 (1995), pp. 590–600.
- [24] Leonard Michael Delves and Julie L Mohamed. *Computational methods for integral equations*. CUP Archive, 1985.
- [25] B Dietz and Achim Richter. “Quantum and wave dynamical chaos in superconducting microwave billiards”. In: *Chaos: An Interdisciplinary Journal of Nonlinear Science* 25.9 (2015).
- [26] Manfredo P Do Carmo. *Differential geometry of curves and surfaces: revised and updated second edition*. Courier Dover Publications, 2016.
- [27] Siegfried Flügge. *Practical quantum mechanics*. Springer Science & Business Media, 2012.
- [28] B Ford. “Numerical solution of integral equations, edited by LM Delves and J. Walsh. Pp 339.£ 4· 50. 1974. SBN 0 19 853342 X (Oxford University Press)”. In: *The Mathematical Gazette* 59.410 (1975), pp. 296–297.
- [29] David J Griffiths and Darrell F Schroeter. *Introduction to quantum mechanics*. Cambridge university press, 2018.
- [30] Thomas Guhr, Axel Müller-Groeling, and Hans A Weidenmüller. “Random-matrix theories in quantum physics: common concepts”. In: *Physics Reports* 299.4-6 (1998), pp. 189–425.
- [31] Martin C Gutzwiller. *Chaos in classical and quantum mechanics*. Vol. 1. Springer Science & Business Media, 2013.
- [32] Fritz Haake. *Quantum signatures of chaos*. Springer, 1991.

- [33] Brian C Hall and Brian C Hall. “The Spectral Theorem for Bounded Self-Adjoint Operators: Statements”. In: *Quantum Theory for Mathematicians* (2013), pp. 131–152.
- [34] Elliott G Holliday, John F Lindner, and William L Ditto. “Solving quantum billiard eigenvalue problems with physics-informed machine learning”. In: *AIP Advances* 13.8 (2023).
- [35] George C Hsiao and Wolfgang L Wendland. *Boundary integral equations*. Springer, 2008.
- [36] WeiHan Hsiao. “Introduction to Classical Chaos”. In: ().
- [37] Yasuhiko Ikebe. “The Galerkin method for the numerical solution of Fredholm integral equations of the second kind”. In: *Siam Review* 14.3 (1972), pp. 465–491.
- [38] Steven G. Johnson. *QuadGK.jl: Gauss–Kronrod integration in Julia*. <https://github.com/JuliaMath/QuadGK.jl>. 2013.
- [39] David L Kaufman, Ioan Kosztin, and Klaus Schulten. “Expansion method for stationary states of quantum billiards”. In: *American Journal of Physics* 67.2 (1999), pp. 133–141.
- [40] Stephen Martin Kirkup and S Amini. “Solution of the Helmholtz eigenvalue problem via the boundary element method”. In: *International Journal for Numerical Methods in Engineering* 36.2 (1993), pp. 321–330.
- [41] VE Kravtsov. “Random matrix theory: Wigner-dyson statistics and beyond.(lecture notes of a course given at sissa (trieste, italy))”. In: *arXiv preprint arXiv:0911.0639* (2009).
- [42] Rainer Kress. *Linear integral equations*. Vol. 82. Springer, 1999.
- [43] Thomas Kriecherbauer, Jens Marklof, and Alexander Soshnikov. “Random matrices and quantum chaos”. In: *Proceedings of the National Academy of Sciences* 98.19 (2001), pp. 10531–10532.
- [44] Shih-Hsien Kuo and Jacob K White. “A Nyström-like Approach to Integral Equations with Singular Kernels”. In: ().
- [45] Jae Weon Lee, Alexei D Chepelianskii, and Dima L Shepelyansky. “Applications of quantum chaos to realistic quantum computations and sound treatment on quantum computers”. In: *Noise and Information in Nanoelectronics, Sensors, and Standards II*. Vol. 5472. SPIE. 2004, pp. 246–251.
- [46] Edward N Lorenz. “Deterministic Nonperiodic Flow 1”. In: *Universality in Chaos, 2nd edition*. Routledge, 2017, pp. 367–378.
- [47] Feng Luo et al. “Application of random matrix theory to biological networks”. In: *Physics Letters A* 357.6 (2006), pp. 420–423.
- [48] Attila Mate. “The frenet-serret formulas”. In: *Brooklyn Collage Of The City University Of New York, izdano* 19 (2017).
- [49] DD de Menezes, M Jar e Silva, and FM de Aguiar. “Numerical experiments on quantum chaotic billiards”. In: *Chaos: An Interdisciplinary Journal of Nonlinear Science* 17.2 (2007).

- [50] Sean Mullane. “Sampling random quantum circuits: a pedestrian’s guide”. In: *arXiv preprint arXiv:2007.07872* (2020).
- [51] James R Nagel. “Introduction to numerical integration”. In: *University of Utah, Salt Lake City, Utah*. URL <http://www.ece.utah.edu/ece6340/LECTURES/Jan30/>. PDF soubor *Numerical Intergation*, posledni pristup 8.5 (2012), p. 2019.
- [52] Kerli Orav-Puurand, Arvet Pedas, and Gennadi Vainikko. “Nyström type methods for Fredholm integral equations with weak singularities”. In: *Journal of Computational and Applied Mathematics* 234.9 (2010). Third International Workshop on Analysis and Numerical Approximation of Singular Problems [IWANASP08], pp. 2848–2858. ISSN: 0377-0427. DOI: <https://doi.org/10.1016/j.cam.2010.01.033>. URL: <https://www.sciencedirect.com/science/article/pii/S0377042710000373>.
- [53] Kerli Orav-Puurand, Arvet Pedas, and Gennadi Vainikko. “Nyström type methods for Fredholm integral equations with weak singularities”. In: *Journal of computational and applied mathematics* 234.9 (2010), pp. 2848–2858.
- [54] Akhilesh Pandey, Avanish Kumar, and Sanjay Puri. “Quantum chaotic systems and random matrix theory”. In: *arXiv preprint arXiv:1905.10596* (2019).
- [55] Théodore Papadopoulo and Manolis IA Lourakis. “Estimating the jacobian of the singular value decomposition: Theory and applications”. In: *Computer Vision-ECCV 2000: 6th European Conference on Computer Vision Dublin, Ireland, June 26–July 1, 2000 Proceedings, Part I* 6. Springer. 2000, pp. 554–570.
- [56] Michael Pasek. “Application of quantum chaos methods to the oscillations of rapidly rotating stars”. In: (2012).
- [57] Andreas Rathsfeld. “Quadrature methods for 2D and 3D problems”. In: *Journal of computational and applied mathematics* 125.1-2 (2000), pp. 439–460.
- [58] M. T. Homer Reid, Steven Johnson, and Jacob White. “Generalized Taylor-Duffy Method for Efficient Evaluation of Galerkin Integrals in Boundary-Element Method Computations”. In: *IEEE Transactions on Antennas and Propagation* 63 (Dec. 2013). DOI: 10.1109/TAP.2014.2367492.
- [59] Ana L Retore. “Introduction to classical and quantum integrability”. In: *Journal of Physics A: Mathematical and Theoretical* 55.17 (2022), p. 173001.
- [60] Achim Richter. *Playing billiards with microwaves—quantum manifestations of classical chaos*. Springer, 1999.
- [61] RW Robinett. *Visualizing the solutions for the circular infinite well in quantum and classical mechanics*. Tech. rep. SCAN-9506104, 1995.

- [62] Marko Robnik. “Classical dynamics of a family of billiards with analytic boundaries”. In: *Journal of Physics A: Mathematical and General* 16.17 (1983), p. 3971.
- [63] Olof Runborg. “Helmholtz equation and high frequency approximations”. In: *KTH Computer Science and Communication, Tech. Rep. DN2255–Numerical Solutions of Differential Equations, Lecture Notes* 5 (2012).
- [64] Jelena Schmalz et al. “On the derivation of the Green’s function for the Helmholtz equation using generalized functions”. In: 78 (Feb. 2010), pp. 181–186. DOI: 10.1119/1.3253655.
- [65] RNL Smith. “Simplifying integration for logarithmic singularities”. In: *WIT Transactions on Modelling and Simulation* 14 (2025).
- [66] Nina Claire Snaith. “Random matrix theory and zeta functions”. PhD thesis. University of Bristol, 2000.
- [67] Hans-Jürgen Stöckmann. “Microwave billiards and quantum chaos”. In: *Scholarpedia* 5.10 (2010), p. 10243.
- [68] Gregor Tanner. “How chaotic is the stadium billiard? A semiclassical analysis”. In: *Journal of Physics A: Mathematical and General* 30.8 (1997), p. 2863.
- [69] Lloyd N Trefethen. “Is gauss quadrature better than Clenshaw–Curtis?” In: *SIAM review* 50.1 (2008), pp. 67–87.
- [70] Francesco Giacomo Tricomi. *Integral equations*. Vol. 5. Courier corporation, 1985.
- [71] Jan Wiersig. “Boundary element method for resonances in dielectric microcavities”. In: *Journal of Optics A: Pure and Applied Optics* 5.1 (2002), p. 53.